Holographic Generation of Arbitrary Intensity Patterns

Jan Adrianus de Haan

Bachelorarbeit in Physik
angefertigt im Institut für Angewandte Physik

vorgelegt der
Mathematisch-Naturwissenschaftlichen Fakultät
der
Rheinischen Friedrich-Wilhelms-Universität
Bonn

August 2022

Ich versichere, dass ich diese Arbeit selbstständig verfasst und keine anderen als die angegebenen Quellen und Hilfsmittel benutzt sowie die Zitate kenntlich gemacht habe.

Bonn, 20. August 2022
Datum

Unterschrift

1. Gutachter: Prof. Dr. Sebastian Hofferberth
2. Gutachter: Prof. Dr. Dieter Meschede

Contents

CHAPTER 1

Introduction

The invention of the laser [1] and the development of laser cooling [2] have led to massive breakthroughs in control over few or even single quanta of matter. A key component of this development is the optical dipole trap [3], which enables confinement of single atoms [4, 5], molecules or even macroscopic structures [6] to regions of high or low intensity of light.

The simplest intensity distribution that is suitable for optical dipole trapping consists of a single focused laser beam. Two crossed laser beams allow tighter confinement in the area where they overlap. More than one trapping site may be created by interference between two counter-propagating laser beams. [7]

More intricate trapping potentials may be created with the aid of acousto-optical deflectors (AODs), digital micromirror devices (DMDs), or liquid crystal on silicon spatial light modulators (LcOS-SLMs). AODs use interactions between phonons and photons in a crystal to deflect laser beams, and are especially well suited for creating arrays of tightly focused traps. DMDs consist of lots of tiny movable mirrors that may be used to apply binary intensity holograms. LcOS-SLMs (from here on called simply SLMs) are made of birefringent liquid crystals that allow applying fairly continuous phase holograms. The latter two devices enable the creation of any tailored intensity pattern in the focal plane of a lens. [8]

This thesis is about setting up an SLM to use in an ultracold atom experiment. The Rubidium Quantum Optics (RQO) experiment in Bonn exploits the possibility of controlling ultracold atoms to manipulate single photons [9, 10], by using collectives of Rubidium atoms in Rydberg states, called Rydberg superatoms. So far, multiple Rydberg superatoms have been created in the experiment using an optical dipole trap with three trapping sites (each containing $\approx 1 \times 10^4$ atoms) that were made by splitting a laser beam with an AOD [11, 12].

In the future, the AOD-generated traps will be replaced by or combined with tailored optical potentials created with an SLM. In this thesis, an SLM is set up and used to create an intensity distribution similar to the one used so far in the RQO experiment.

In chapter 2, the mechanism of image creation with the SLM is described by modeling it using the theory of scalar diffraction. Methods of finding phase patterns to display on the SLM to achieve tailored potentials are discussed.

The methods from chapter 2 are used in chapter 3 to compute a phase pattern that creates three tightly focused spots. It is displayed on the SLM, in an optical setup similar to the one that will be used when the SLM is employed in the RQO experiment. The measured intensity pattern is characterized

considering its application for trapping atoms, with regards to the created spots' shapes and intensities, and with regards to background intensity and stray spots, as well as diffraction efficiency in different areas of the image. The aberrations of the optical system are measured and corrected for using the SLM. A method for iteratively improving the evenness of the spots in the intensity pattern is implemented.

After the characterization, steps towards implementing the SLM in the RQO experiment are described in chapter 4. The setup of the laser that will provide the light for the SLM- and perhaps additional AOD-traps is described. The intensity outside the focal plane is measured and calculated. The intensity distribution is used to simulate trapping potentials and atomic distributions. The latter allow comparing the SLM traps to the AOD-traps that were used before. Finally, the SLM's ability to move the focal plane is evaluated as a possible alignment method.

CHAPTER 2

Computing phase patterns to display on the SLM for given intensity patterns

The first step towards generating arbitrary intensity patterns using an SLM is to understand how they are created. The SLM does not change the intensity of a beam, but adds a phase pattern to the field. When focused with a lens, the field interferes to create an intensity pattern. This chapter covers the theoretical background for generating tailored intensity patterns with an SLM.

First, the ability of a lens to perform an optical Fourier transform will be derived in section 2.1. The working principle of an SLM is discussed in section 2.2, and is used to a derive the image that an ideal SLM would produce when displaying a phase pattern. The result leads to different methods of phase retrieval, which are discussed in section 2.3. Finally, the effects of differences of the real system from an idealized SLM and lens are treated in section 2.4.

2.1 Intensity distribution in the focal plane of a lens

Figure 2.1 shows a lens in a coordinate system. If the electromagnetic field propagating in the z-direction is known in front of the lens, it is possible to calculate the field at any point behind the lens. Doing this will be necessary in order to describe what happens when an SLM imprints a phase pattern onto an electromagnetic field. The entire following derivation is a summary of the relevant points of chapter 3 and 4 of ref. [13]. Its purpose is to clearly state the assumptions underlying the calculation of phase patterns to display on the SLM.

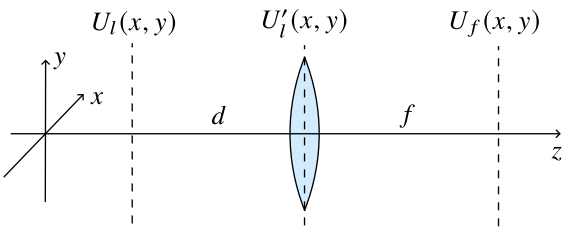

Figure 2.1: The propagation of light through a lens is described using scalar fields U_l, U_l' and U_f in the input, lens and focal planes. The distance between the input and lens planes is d, the distance between the lens and the focal plane is f.

The light propagating from the input plane to the focal plane through the lens is described as a scalar field. This means that the electric and magnetic vector fields obeying the Maxwell equations are replaced by a single component u of the electric or

magnetic vector fields, obeying the wave equation

$$\nabla^2 u - \frac{n^2}{c^2}\frac{\mathrm{d}^2 u}{\mathrm{d}t^2} = 0.$$

The scalar field description is justified by the fact that, in media such as air or glass, all components of both vectors obey this same wave equation. This simplification approximates the results obtained using the full vector field description very well in the limit of diffracting structures which are much larger than the light's wavelength. [13, pp. 35ff.] Since the time dependency of u is purely harmonic, i.e. $u(P,t) = A(P)\cos(2\pi\nu t - \phi(P))$ at a location P, the field is fully described by a complex time-independent field $U = A(P)e^{i\phi(P)}$, which must then obey the Helmholtz equation

$$(\nabla^2 + k^2)U = 0 \tag{2.1}$$

with $k = 2\pi n\nu/c = 2\pi/\lambda$.

Let U be the field in an aperture, and U' the field at a distance z from that aperture. The field U' may then be calculated using the Huygens-Fresnel principle

$$U'(x,y) = \frac{z}{i\lambda}\iint U(\xi,\eta)\frac{\exp(ikr_{01})}{r_{01}^2}\,\mathrm{d}\xi\,\mathrm{d}\eta\,.$$

It states that the field at any point in the plane is given by the superposition of spherical waves emitted from the input plane. Here, $r_{01} = \sqrt{z^2 + (x-\xi)^2 + (y-\eta)^2}$ is the distance between the point (x,y) in the image plane and the point (ξ,η) in the aperture plane.

To ease the computation of this integral, the square root is approximated using the first two terms of its Taylor series as $\sqrt{1+b} \approx 1 + b/2$. In the denominator, only the first term is used, since compared to the exponential term, it is much less sensitive to changes in r_{01}. This yields the integral in Fresnel-approximation

$$\begin{aligned} U'(x,y) &= \frac{e^{ikz}}{i\lambda z}\iint U(\xi,\eta)\exp\left(\frac{ik}{2z}\left[(x-\xi)^2 + (y-\eta)^2\right]\right)\mathrm{d}\xi\,\mathrm{d}\eta \\ &= \frac{e^{ikz}}{i\lambda z}e^{\frac{ik}{2z}(x^2+y^2)}\iint U(\xi,\eta)e^{\frac{ik}{2z}(\xi^2+\eta^2)}e^{-i\frac{2\pi}{\lambda z}(x\xi+y\eta)}\,\mathrm{d}\xi\,\mathrm{d}\eta\,. \end{aligned} \tag{2.2}$$

The approximation is valid for the system considered here, even though the errors of the Taylor expansion would suggest otherwise [13, pp. 66ff.]. In the first form, the integral states the Huygens-Fresnel principle with quadratically approximated spherical waves. The second form is useful for the following calculation.

In this formalism, the effect of a lens of focal length f is the multiplication of the field with the phase factor $\exp\left(-\frac{ik}{2f}(x^2+y^2)\right)$. In the paraxial approximation, this phase factor turns a plane wave into a converging or diverging spherical wave (depending on the sign of f). It may be derived explicitly by considering the geometry of a spherical lens [13, pp. 97ff.]. Systems of lenses may be described using the same phase factor, since multiplying the phase factors of two lenses with focal lengths f_1 and f_2 leads to a phase factor of the same structure but with a different focal length $f = \frac{1}{1/f_1+1/f_2}$.

If the input field of a lens is U_l, the field behind the lens is $U_l'(x,y) = U_l(x,y)e^{-\frac{ik}{2f}(x^2+y^2)}$. Using

this as the input field to the Fresnel diffraction formula 2.2 leads to the following output field at a distance of $z = f$ from the lens.

$$\begin{aligned} U_f(x,y) &= \frac{\exp\left(-\frac{ik}{2f}(x^2+y^2)\right)}{i\lambda f} \iint U_l'(\xi,\eta) \exp\left(\frac{ik}{2f}(\xi^2+\eta^2)\right) \exp\left(-\frac{2\pi i}{\lambda f}(x\xi+y\eta)\right) \mathrm{d}\xi\, \mathrm{d}\eta \\ &= \frac{\exp\left(-\frac{ik}{2f}(x^2+y^2)\right)}{i\lambda f} \iint U_l(\xi,\eta) \exp\left(-\frac{2\pi i}{\lambda f}(x\xi+y\eta)\right) \mathrm{d}\xi\, \mathrm{d}\eta \end{aligned} \tag{2.3}$$

Because the terms containing $(\xi^2+\eta^2)$ from the Fresnel integral and the lens phase cancel, this is the Fourier Transform $\mathcal{F}[f](x,y) = \iint f(\xi,\eta) e^{-2\pi i(\xi x+\eta y)} \,\mathrm{d}\xi\, \mathrm{d}\eta$ of the input field, except for a constant phase factor. The constant phase factor is irrelevant for the intensity, which is given by

$$I_f(x,y) = \frac{1}{\lambda^2 f^2} \left| \mathcal{F}[U_l]\left(\frac{x}{\lambda f}, \frac{y}{\lambda f}\right)\right|^2 .$$

This is the property of a lens that will be used to create arbitrary intensity patterns using the SLM by varying the input phase $\phi(x,y)$ of the input field $U_l(x,y) = A_l(x,y)e^{i\phi(x,y)}$.

2.2 Image created by an ideal SLM

Liquid Crystal on Silicon Spatial Light Modulators (LcOS-SLM) are made of a layer of birefringent liquid crystals on top of a mirror substrate. The surface of the SLM is divided into pixels. At each pixel, the orientation of these crystals may be changed by applying a voltage. The change in orientation of the birefringent crystals alters the refractive index of the pixel. The SLM is manufactured such that the liquid crystal layer's thickness allows imprinting a phase shift between 0 and 2π. The SLM used in this thesis[1] has 792×600 square pixels of side length 12.5 µm.

The image is produced in the focal plane of a lens positioned behind the SLM displaying a phase pattern. Finding phase patterns that produce a target image when displayed on the SLM requires calculating the intensity a given phase pattern displayed on the SLM produces. This is done by applying the result from section 2.1 to the field produced by an ideal SLM when illuminated with a plane wave.

For an SLM of $N_x \times N_y$ pixels with pixel size $d_x \times d_y$, which is imposing the phase ϕ_{nm} on the light hitting the pixel (n,m), the input field is

$$U_l(x,y) = \sum_{n=0}^{N_x-1} \sum_{m=0}^{N_y-1} e^{i\phi_{nm}} \operatorname{rect}(x/d_x - n - N_x/2) \operatorname{rect}(y/d_y - m - N_y/2),$$

[1] Hamamatsu LcOS-SLM X13267-02

when the center of the SLM is located at the origin. Here, the rectangular function is defined as

$$\mathrm{rect}(x) = \begin{cases} 1 & -1/2 \leq x \leq 1/2 \\ 1/2 & |x| = 1/2 \\ 0 & \text{otherwise} \end{cases}.$$

Non-quadratic pixels are an interesting case to treat even if the SLM's pixels are quadratic because the pixels effectively become non-quadratic for a non-zero angle of incidence.

To compute the output field, note that the Fourier transform of the rectangular function is $\mathcal{F}[\mathrm{rect}(\xi)](x') = \mathrm{sinc}(x')$. Also, for any function f, the Fourier transform has the property $\mathcal{F}[f(a\xi - b)](x') = \mathcal{F}[f(\xi)](x'/a)e^{-2\pi i b x'/a}/|a|$. In the following, $x' = \frac{x}{\lambda f}$ and $y' = \frac{y}{\lambda f}$ are the Fourier-space coordinates. Using eq. 2.3, the output field is thus given by

$$\begin{aligned} U_f(x,y) &= \frac{d_x d_y}{\lambda f} \sum_{n=0}^{N_x-1} \sum_{m=0}^{N_y-1} e^{i\phi_{nm}} \,\mathrm{sinc}(x' d_x)\,\mathrm{sinc}(y' d_y) e^{-2\pi i((n+N_x/2)d_x x' + (m+N_y/2)d_y y')} \\ &= \frac{d_x d_y}{\lambda f} \,\mathrm{sinc}\left(\frac{x}{L_x}\right) \mathrm{sinc}\left(\frac{y}{L_y}\right) e^{-\pi i(N_x d_x x' + N_y d_y y')} \sum_{n=0}^{N_x-1} \sum_{m=0}^{N_y-1} e^{i\phi_{nm}} e^{-2\pi i(n N_x d_x x'/N_x + m N_y d_y y'/N_y)} \\ &= \frac{d_x d_y}{\lambda f} \,\mathrm{sinc}\left(\frac{x}{L_x}\right) \mathrm{sinc}\left(\frac{y}{L_y}\right) e^{-i\phi_0(x,y)} \,\mathrm{DFT}[e^{i\phi}]\left(\frac{x}{L_x}N_x, \frac{y}{L_y}N_y\right) \end{aligned} \tag{2.4}$$

where $L_x = \lambda f/d_x$ and $L_y = \lambda f/d_y$ are the dimensions of the image, and the 2D Discrete Fourier Transform of an $N_x \times N_y$ matrix with entries A_{nm} is defined as

$$\mathrm{DFT}[A](k,l) = \sum_{n=0}^{N_x-1} \sum_{m=0}^{N_y-1} e^{-2\pi i(kn/N_x + lm/N_y)} A_{nm}.$$

If we allow k and l to be real numbers, equation 2.4 is exact. Note that k and l may also be negative, but that the DFT values are periodic in the number of pixels N_x or N_y respectively, and may thus be computed using $k + N_x$ or $l + N_v$ respectively.

The SLM can be modeled differently. In refs. [14, pp. 92f.] and [15, pp. 43f.], the image plane is divided into focal units whose size is determined by the size of the SLM, and the field at each pixel is approximated as a δ-peak. This approach also yields the DFT as the solution.

2.3 Methods of phase retrieval

In the previous section, the DFT was shown to describe the intensity pattern corresponding to a given phase pattern. We would now like to do the inverse: Find a phase pattern that yields a given intensity pattern. Since the SLM only allows altering the phase of light, the amplitude of the field is fixed, which prevents simply displaying the inverse Fourier transform of a target intensity pattern.

There are multiple ways of finding an applicable phase pattern. The SLM may simply be used as a phase grating, but more intricate patterns may be achieved with more complicated phase patterns.

2.3.1 Gratings

Very simple patterns may be produced by using the property $\mathcal{F}[f(x,y)e^{i(ax+by)}](\xi,\eta) = \mathcal{F}[f(x,y)](\xi-a,\eta-b)$ of the Fourier Transform, by applying a phase grating with slopes a and b in the x and y directions. This shifts the resulting image proportionally to the slopes. For a slope a, the resulting shift of the image is $\lambda f a$.

This approach may be used to shift a more complex pattern or, if nothing else is displayed but these gratings on different areas of the SLM, create spots at different locations by turning the SLM into a beam splitter [14, p. 94].

2.3.2 Iterative Fourier transform algorithms (IFTA)

The beam-splitter approach is unsuitable for images that are not just spot arrays. Even for such target images, the following approach is preferred in literature [14, 15]. A phase pattern that yields an image of interest may be computed iteratively. This can be done using a class of algorithms called iterative Fourier transform algorithms (IFTA). The general structure of such an algorithm is as follows, given the intensity I_0 incident on the SLM (see also figure 2.2):

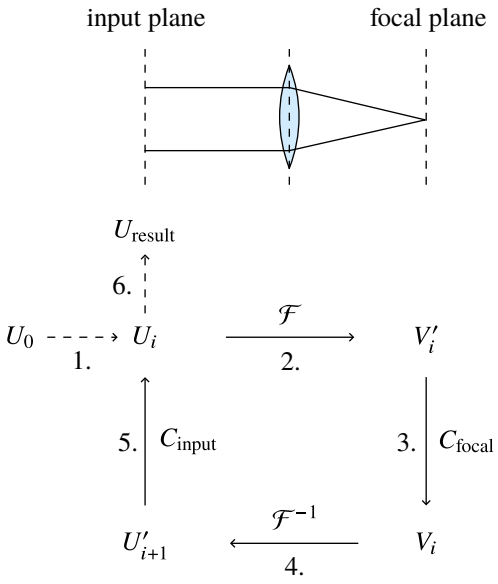

Figure 2.2: Diagram of an Iterative Fourier Transform Algorithm (IFTA). Starting in the input plane, the field is propagated back and forth between the focal plane and the input plane of a lens using the (inverse) Fourier Transform $\mathcal{F}$ and $\mathcal{F}^{-1}$, and constraints C_{input} and C_{focal} are enforced in both planes. This figure is based on the ones in refs. [14–17].

1. Start with an initial field in the input plane $U_0 = A_0 e^{i\phi_0}$ where $A_0 = \sqrt{I_0}$.
2. Fourier-transform the field U_i to obtain the field V_i' in the focal plane: $V_i' = \mathcal{F}[U_i]$
3. Constrain the field in the focal plane: $V_i = C_{\text{focal}} V_i'$
4. Inverse Fourier-transform this field to obtain a field that would yield this constrained field: $U_{i+1}' = \mathcal{F}^{-1}[V_i]$
5. Constrain the input field: $U_{i+1} = C_{\text{input}} U_{i+1}'$
6. Repeat starting at the the second step, unless the intensity in the focal plane is sufficiently close to the target intensity.

An IFTA-variant consists of the two constraint operators C_{input} and C_{focal}, as well as a starting phase ϕ_0. The variant that will be used here is the Gerchberg-Saxton algorithm (described originally in ref. [18]). For this variant, the constraint in the input plane is keeping the phase and changing only the intensity, i.e. $C_{\text{input}}(Ae^{i\phi}) = \sqrt{I_{\text{in}}} e^{i\phi}$, and the constraint in the focal plane is keeping the phase

and changing the intensity to the target intensity, i.e. $C_{\text{focal}}(Ae^{i\phi}) = \sqrt{I_{\text{target}}}e^{i\phi}$. The starting phase is chosen to be random.

Other variants of this algorithm are better suited for phase patterns containing large flat areas (see e.g. ref. [19], or for an implementation of a variant ref. [16]), or can be used to correct for aberrations of the optical system (see ref. [14, pp. 110ff.]).

2.3.3 Numerical implementation

Using the result from section 2.2, the field in the focal plane is computed using the DFT of a matrix of size $N_x \times N_y$ which contains the phases of each pixel. If the DFT had to be computed using the Fast Fourier Transform (FFT) algorithm, the SLM's resolution of 792×600 would pose a problem, since it is not a power of two, severely reducing the efficiency of the FFT.

Ref. [15] solves this problem by zero-padding to the next power of two, but notes that better results were achieved using even larger matrices. Refs. [16] and [17] use matrices whose size is the first power of two larger than $2N_x$ and $2N_y$, since the Nyquist sampling theorem states that a field with maximum spatial frequency ξ may be fully reproduced when sampled at a frequency greater than 2ξ. The infinite frequencies necessary for perfectly sharp pixel edges may be disregarded, since the transition between the phase shift imposed onto the light between two pixels is not perfectly sharp anyway [20].

In this thesis, the IFTA is implemented in Python using Scipy. Scipy includes an implementation of Bluestein's algorithm, which allows efficiently ($O(n \log n)$, just like the FFT) calculating the DFT for matrices of any size. This allows calculating the Fourier transform using a DFT of a matrix of size $N_x \times N_y$ directly.

Since the result in section 2.2 was exact for non-integer arguments to the DFT, it permits efficient computation of the expected image at a a resolution higher than that of the SLM. This is done by realizing that for integer k and l and $\delta, \epsilon \in [0, 1]$,

$$\begin{aligned}
\text{DFT}[A](k+\delta, l+\epsilon) &= \sum_{n=0}^{N_x-1} \sum_{m=0}^{N_y-1} e^{-2\pi i((k+\delta)n/N_x + (l+\epsilon)m/N_y)} A_{nm} \\
&= \sum_{n=0}^{N_x-1} \sum_{m=0}^{N_y-1} e^{-2\pi i(\delta n/N_x + \epsilon m/N_y)} e^{-2\pi i(kn/N_x + lm/N_y)} A_{nm} \\
&= \text{DFT}[A'](k, l)
\end{aligned}$$

with $A'_{nm} = e^{-2\pi i(\delta n/N_x + \epsilon m/N_y)} A_{nm}$. This means that the same algorithm used for computing the DFT before can be applied to a matrix whose entries are multiplied by certain phase factors. To compute the image at a resolution higher than that of the SLM, one computes $\text{DFT}[A](k+\delta, l+\epsilon)$ for different values of δ and ϵ, e.g. $\delta, \epsilon \in \{0, 1/2\}$ for two times the resolution along both axes, and intersperses the four resulting matrices.

2.4 Differences from the ideal system

All discussion to this point has considered an ideal SLM and lens, but the intensity pattern that can be obtained in the experiment is influenced by various differences of the real system from the one so far

considered. A list of them (which is not claimed to be complete) follows. Most of these effects have been observed in the measurements made in chapter 3.

Zeroth-order spot While an ideal SLM would impose a given phase onto all the light that hits it, this is not the case for a real SLM, which leaves some of the reflected light unperturbed. This is e.g. due to some of the light being reflected by the glass in front of the liquid crystals, or due to the pixels not filling the entire area of the SLM, leaving gaps inbetween. The unaltered light leads to a zeroth-order spot in the middle of images produced with the setup. Some applications may require this spot to be blocked.

Mismatch between design-wavelength and used wavelength The SLM used in this thesis is designed to be used at a wavelength of 785 nm, but is used at 805 nm. Thus, the longer wavelength light never experiences a 2π phase shift, but instead at most 97.5 % of that.

Additional diffraction orders of gratings Any grating displayed on the SLM will, due to the finite number of pixels, not be perfectly smooth but rather a multi-level phase grating. While a perfectly smooth grating would yield a single diffraction order, which just appears as a shifted image, a multilevel phase grating has more than one diffraction order. The minus first diffraction order is visible as a mirrored copy of any off-center image displayed on the SLM.

Copies of the image The finite pixel size of the SLM leads to multiple copies of the entire image (which includes the copies due to the pixelated gratings used to shift images inside the image region) being visible: There are multiple diffraction orders spaced $L = \lambda f / d$ apart, in two directions, where d is the pixel size in that direction.

Non-zero angle of incidence If a beam of light is incident on the SLM at an angle θ different from 0, the beam interacts with the projection of each pixel onto the plane perpendicular to the beam, effectively reducing the pixel size to $\tilde{d}_x = d_x / \cos\theta$. This increases the image size in that direction to $\tilde{L}_x = \lambda f / \tilde{d}_x = L_x / \cos\theta$. To compensate for this, the center $\cos\theta$ part of the phase pattern that would be displayed for $\theta = 0$ can be stretched to fill the entire SLM. Apart from interpolation effects, this compensates for the incidence angle.

Uneven SLM-surface The SLM's surface is not perfectly even. The manufacturer provides a measurement of this unevenness in the form of a phase pattern that may be displayed on the SLM to compensate for the unevenness.

Aberrations of lenses In addition to the effects introduced by the non-ideal SLM, real lenses also introduce deviations of the target image from the ideally expected one. These differences, caused e.g. by the paraxial approximation not holding perfectly, are called aberrations. They may be described as an additional phase imprinted on the field when passing through the lens. Certain common aberrations are described using Zernike polynomials, which form an orthonormal basis of the unit disk. The first Zernike polynomials correspond to named aberrations, such as tilt, coma or astigmatism.

If the differences between an expected wavefront and the real wavefront can be measured, the difference can be displayed in reverse on the SLM to correct for the aberrations, since the resulting wave will then be exactly what the perfect optical system would have produced.

One way of measuring the wavefront is using a Shack-Hartmann sensor, which consists of a camera with a microlens array in front such that the foci are in the camera plane. When a tilted wavefront hits a microlens, the focused spot is displaced. The wavefront's tilt can be deduced from the spot's displacement. The wavefront itself is then the scalar field whose gradient is the wavefront tilt at each point. This implies that the wavefront is only defined up to a constant, which makes sense, since constant phase shifts are irrelevant.

CHAPTER 3

Characterization and improvement of spot patterns

In this chapter, the Gerchberg-Saxton algorithm described in chapter 2 is used to calculate a phase pattern which produces three spots focused as tightly as possible, with the lower limit given by the SLM's dimensions and the size of the beam used to illuminate it. This target pattern has been chosen because it resembles the three beams from an AOD which has previously been used in the RQO experiment for trapping ultracold atoms. three spots created using an AOD have been used in the RQO experiment before to alter the dipole trapping potential for the atoms. The performance of the SLM is tested with a 79.5 mm focal length objective from the RQO experiment with an additional telescope with magnification 4 in front. The phase pattern is chosen such that the distance between the spots is 50 µm with this lens system.

The relevant part of the experimental setup used to create the intensity pattern and take images of it, as well as calibration measurements performed, are described in section 3.1. The preparation of the displayed phase pattern is described in detail in section 3.2. The intensity patterns that are measured when this phase pattern is displayed on the SLM are characterized in section 3.3. The characterization is performed considering the application of the intensity pattern for altering a dipole trapping potential for Rubidium atoms. Finally, the iterative improvement of the evenness of the spots' intensities is described in section 3.4.

3.1 Experimental setup

The experimental setup has two parts. The first one consists of the laser and various optics required to adjust polarization and power of the beam. The beam is coupled into a fiber, which leads to the second part of the setup. The second part contains the SLM itself, a lens, and an imaging setup. The first part will be discussed in detail in section 4.1. For this chapter, it is only relevant that a beam of horizontally linearly polarized 805 nm light comes out of the fiber outcoupler at the start of the measurement setup.

The second part of the setup is shown in figure 3.1. The beam is coupled out of the fiber with an outcoupler with a lens of focal length 11 mm. It is widened using a telescope consisting of two lenses with focal lenghts $f = -50\,\text{mm}$ and $f = 200\,\text{mm}$ to illuminate a larger area of the SLM. Behind the telescope, the beam waist is $w = (2.28 \pm 0.04)\,\mu\text{m}$, which is determined by taking a beam profile with a camera at different positions. After being reflected from the SLM, the beam is focused onto

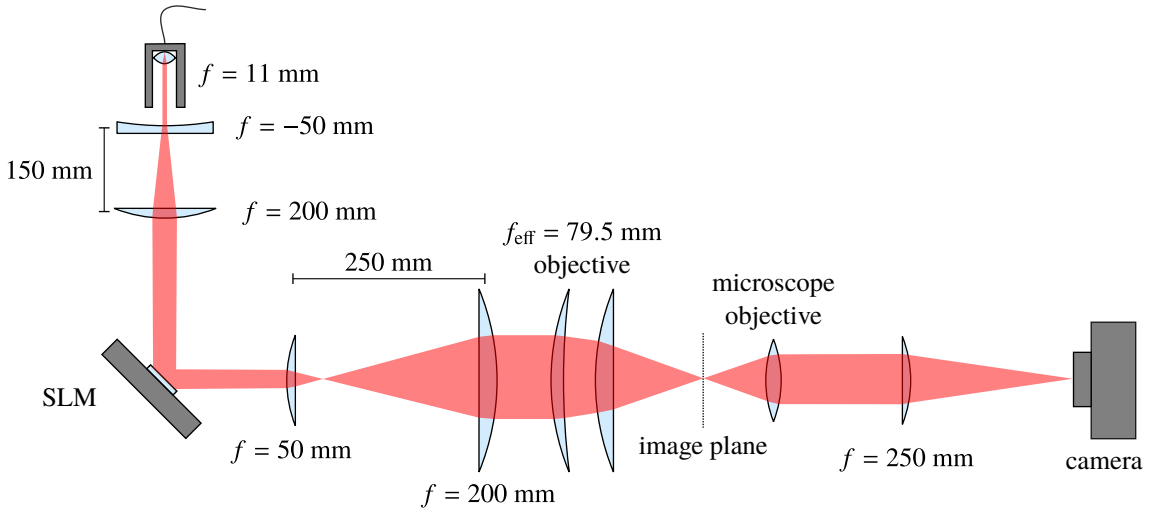

Figure 3.1: The beam from the fiber-outcoupler is enlarged by a factor of 4 using a telescope to a waist of $w = (2.28 \pm 0.04)\,\mu\text{m}$. It is then reflected by the SLM. To obtain more tightly focused spots, the beam is enlarged again using another telescope. Together with the objective of effective focal length $f_{\text{eff}} = 79.5\,\text{mm}$, which is made of two lenses, it forms a system with an even smaller focal length. The reduction in focal length reduces the image size as well as the smallest achievable spot size by a factor of 4. The images that are created in the focal plane of the objective are captured using a microscope. The microscope is made of a microscope objective and a lens with focal length $f = 250\,\text{mm}$. It magnifies a section of the image onto the camera.

the image plane. This is done using an objective, consisting of two lenses, that has been used in the experiment previously. It is proceeded by a telescope made of lenses with focal lengths $f = 50\,\text{mm}$ and $f = 200\,\text{mm}$ to allow sufficiently tightly focusing beams. The objective as well as the second lens of the telescope in front of it are 50.8 mm instead of 25.4 mm in diameter to accommodate the large beam diameter.

A camera[1] is used to image the obtained intensity patterns. It may either be placed directly in the image plane, or, to image in more detail, behind a microscope. The latter is necessary to measure spot profiles, since the camera's pixel size is 6 µm, but the setup allows focusing beams down to waists of 2 µm.

The large angle of incidence between the light and the SLM in this setup was chosen because it allows for a smaller distance between the SLM and the lens compared to small angles of incidence. The latter required, due to the size of the objective and the last lens in front of the SLM, a distance of approximately 50 cm between the SLM and the objective, reducing the image size[2].

A setup that avoids large angles of incidence without requiring a large distance between the SLM and the objective may be realized using a beam splitter in front of the SLM, though this cuts the

[1] Arducam MT9V022 with 640×480 pixels

[2] Ref. [14, pp. 93f.] derives: The circular area limiting the image size has radius $r_v = \frac{f}{2L}\left(D - \sqrt{l_x^2 + l_y^2}\right)$, where f is the focal length of the lens, D is its diameter, L is the distance between SLM and lens, and l_x and l_y are the dimensions of the SLM. While this relationship could not be verified in detail, likely due to additional mirrors in the setup while trying to do so, the image was severely clipped in the small angle-of-incidence setup with the objective, and this issue was resolved when switching to the large angle-of-incidence setup.

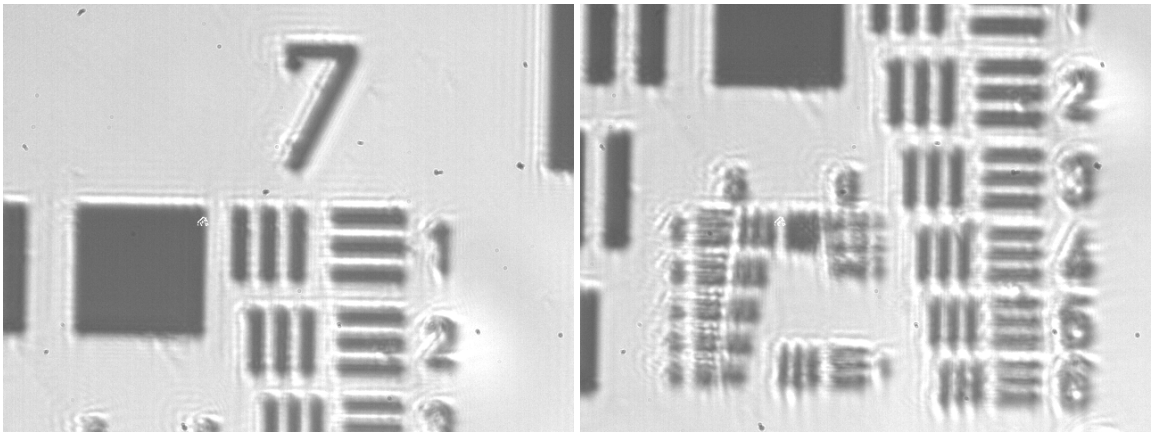

Figure 3.2: Images of the test target captured using the microscope with illumniation by an LED flashlight. Two images were needed to capture the entire group 7 of the test target, the first subgroup is only visible on the first image, the second to 6th groups are visible on the second image.

	expected	vertical		horizontal	
Group	spacing / µm	spacing / mm	magnification	spacing / mm	magnification
1	7.81	0.194	24.87	0.195	24.92
2	6.94	0.176	25.41	0.174	25.02
3	6.21	0.158	25.38	0.154	24.80
4	5.52	0.140	25.34	0.137	24.77
5	4.93	0.128	25.99	0.122	24.70
6	4.39	0.111	25.33	0.108	24.57

Table 3.1: The spacing of lines in the test target groups is determined from the images shown in figure 3.2, the magnification is computed as the ratio between the measured spacing and the real spacing on the test target.

efficiency of the entire setup in half.

Calibration

Before the intensity patterns captured with the camera can be analyzed, the microscope magnification and the camera power response must be calibrated. For later correction with the SLM, the aberrations introduced by the lenses are measured.

Microscope magnification To determine the magnification of the microscope, a USAF-1951-test-target was imaged, using light from an LED flashlight instead of laser light to avoid interference effects which might make the resolution worse.

To accurately determine the magnification, three equally spaced Gaussian functions with background are fitted to each of the subgroups visible in figure 3.2. Even though they do not describe the exact shape of the intensity profiles particularly well, this method does lead to plausible results for the distances between the minima. The spacing that is found is compared with the real spacing of the features on the test target, which is provided by its manufacturer [21]. Both spacings and their ratio, the magnification, are given in table 3.1.

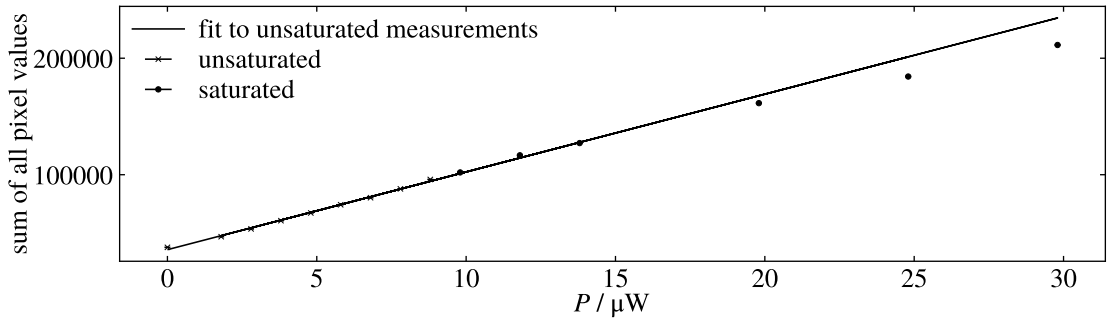

Figure 3.3: Sum of all pixel values at different laser beam powers shone onto the camera. The fit is only performed for the unsaturated measurements. All measurements where any pixel has the maximum value are considered to be saturated. The slope of the line is $(6.67\pm0.14)\times10^{3}\ \mu W^{-1}$ and its y-intercept is $(3.57\pm0.08)\times10^{4}$.

The infinity-corrected objective is intended to be used with a tube lens of focal length 200 mm. In that case it has a magnification of 20. Since a lens of focal length 250 mm is used instead, the expected magnification is 25. It is included in the range of measured magnifications of the different test target features. Thus, from here on, a magnification of 25, in both directions, will be used.

Camera pixel values and power A laser beam of varying power, up to 30 µW, is shone onto the camera, in the same configuration as in later measurements. The background light is measured to be 0.2 µW and is subtracted from the power of the laser beam. The pixel values are normalized to 1 and added up. Whether a measurement was saturated was determined by whether any pixel in the image was 1. Assuming a linear response of the camera, a linear function is fitted to the unsaturated measurements. Since the amount of background light depends on the exact ambient conditions, only the slope of the calibration will be used. The recorded measurements along with the fitted line are shown in figure 3.3. From the slope, the power per pixel value, for pixel values between 0 and 1 is $(1.50\pm0.03)\times10^{-4}$ µW.

Measurement of optical aberrations A Shack-Hartmann sensor[3] is placed behind the objective, at a distance such that the beam fills an area of the sensor that is as large as possible while not being clipped. The software included with the sensor fits Zernike-polynomials to the measured wavefront. Since the Zernike-polynomials are defined on the unit disk, only the part of the wavefront inside the waist

n	m	coefficient (phase shift)
0	0	143.9
1	−1	−8.4
1	1	84.2
2	−2	−0.6
2	0	−226.8
2	2	−0.7
3	−3	−7.4
3	−1	8.7
3	1	0.4
3	3	1.7
4	−4	1.5
4	−2	−0.5
4	0	4.9
4	2	−6.3
4	4	5.3

Table 3.2: These are the Zernike coefficients obtained from the software included with the wavefront sensor. A table of Zernike polynomials is included in the appendix to clarify the indexing scheme (table A.1).

[3] Thorlabs WFS150-5C

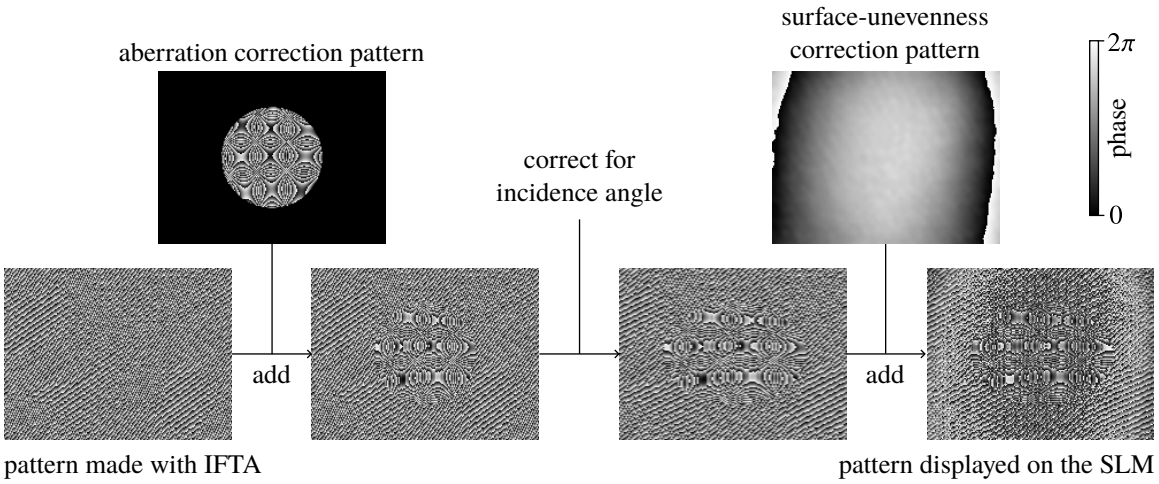

Figure 3.4: A phase pattern computed with the Gerchberg-Saxton algorithm is modified by adding an aberration correction phase pattern, which is obtained by measuring aberrations using a wavefront sensor. The phase pattern is stretched to correct for the 45° angle of incidence. A surface unevenness correction pattern is added to it. Note that the phase patterns above are made for an SLM with a quarter of the resolution of the one actually used, but with 4 times larger pixels. This is done because the phase pattern's structure would be hard to see at the size at which they are shown above, if there were more pixels.

of the beam is considered. The results are given in table 3.2, where the coefficients are given as phases.

The coefficients with indices $(0,0)$, $(1,-1)$, $(1,1)$ and $(2,0)$ are set to zero, because they correspond to a constant phase shift, a tilt of the sensor horizontally or vertically, and the divergence of the beam. The constant phase shift is irrelevant for correcting aberrations, and the tilts are not a property of the optical system, but of the sensor placement. The divergence is to be expected since the beam is not collimated again behind the objective, and should not be corrected for.

The linear combination of Zernike polynomials with these coefficients is the phase pattern that is imposed onto the beam by deviations of the optics from their ideal behavior. An aberration correction phase pattern is made by taking the negative value of the phase introduced by the aberrations, modulo 2π. Since it is circular, with a radius equal to the waist of the beam, it is displayed in the middle of the SLM. Outside the circle, the SLM imposes a phase shift of zero.

3.2 Phase pattern

The process of creating a phase pattern that, when displayed on the SLM, yields an image as similar as possible to the one an ideal SLM with an ideal lens would create, includes some steps after the phase pattern computation using the Gerchberg-Saxton algorithm as described in section 2.3. An example is shown in figure 3.4.

The first step after the initial phase pattern is computed is the addition of the aberration correction pattern. It is made using the measurement described in section 3.1. Since the angle of incidence is $\theta = 45°$, the center $\cos\theta = 1/\sqrt{2}$ part of this phase pattern is taken and stretched to the full size of the SLM by linear interpolation. Note that the aberration correction pattern has also been stretched, which is necessary to ensure that the phase imprinted onto the beam actually corresponds to the aberrations

of the wavefront in that part of the beam. After also adding the surface unevenness correction pattern provided by the manufacturer, the phase pattern is ready to be displayed on the SLM.

3.3 Measured intensity patterns

In this section, intensity patterns are characterized considering their intended use to create an optical dipole trapping potential for Rb-87 atoms. Since the trapping potential is proportional to the intensity (see section 4.3 for details), spots that are as tightly focused and as bright as possible are desirable to create deep traps. The spots should not have multiple minima to avoid multiple atom density maxima where only one is desired. The spot profiles are thus investigated in section 3.3.1. Total background intensity should be as low as possible because any intensity in the background is wasted. If it is not evenly distributed, it might even cause unwanted trapping minima in the potential. These two aspects of the background intensity are investigated in section 3.3.2. The minimum distance necessary between two spots for them to still be usable as distinct traps is measured in section 3.3.3. Intensity patterns generated far off-axis are limited in intensity by the diffraction efficiency of the SLM. The diffraction efficiency is measured in section 3.3.4. Finally, all these characterizations are done both with and without the aberration correction pattern. Its effects are investigated throughout and summarized in section 3.3.5.

3.3.1 Spot profiles

The lower limit of the waists of the spots created is given by the SLM's dimensions and the waist of the beam illuminating the SLM.

The limit given by the SLM dimensions is derived from the structure of the SLM-image shown in section 2.2. The image is given by a DFT at the resolution of the SLM, so the smallest image unit in the x-direction has size $L_x/N_x = \lambda f/(L_x d_x) = \lambda f/l_x$, where $L_x = \lambda f/d_x$ is the image size, N_x is the number of pixels of the SLM, and $l_x = N_x d_x$ is the SLM size. The y-direction is derived analogously. For the SLM used, at the 45° angle of incidence, with a 79.5 mm objective and a 4 times magnifying telescope in front, this limit is 2.29 µm in the x-direction and 2.13 µm in the y-direction.

The waist of a focused Gaussian beam may be computed as $w' = \lambda f/(\pi w)$ [22, p. 54], where w is the waist in front and w' the waist behind the lens. For the lenses used and a (2.23±0.04) mm waist input beam, the beam waist behind the objective is $w = (2.28 \pm 0.04)$ µm, yielding a similar limit as the SLM's dimensions.

The following measurement will determine whether the spots in the intensity pattern actually reach these limits.

In figure 3.5, beam profiles taken with and without the aberration correction phase pattern are shown. The spot waists without the aberration correction pattern are (6.2±0.2) µm in the x- and (3.5±0.1) µm in the y-direction, which is 2.7 and 1.5 times as large as the theoretical limit respectively. The aberration correction pattern does not seem to have the effect of making the beam more focused in both directions: It leads to beam waists of (2.2±0.1) µm and (5.4±0.2) µm in the x- and y-directions respectively. The waist is reduced in the x-direction, but increased in the y-direction. In the x-direction, the theoretical limit is actually achieved.

The shape of the spot is closer to a Gaussian when the aberration correction phase pattern is applied. However, it also severely reduces the intensity of the beams, which is the opposite of what would

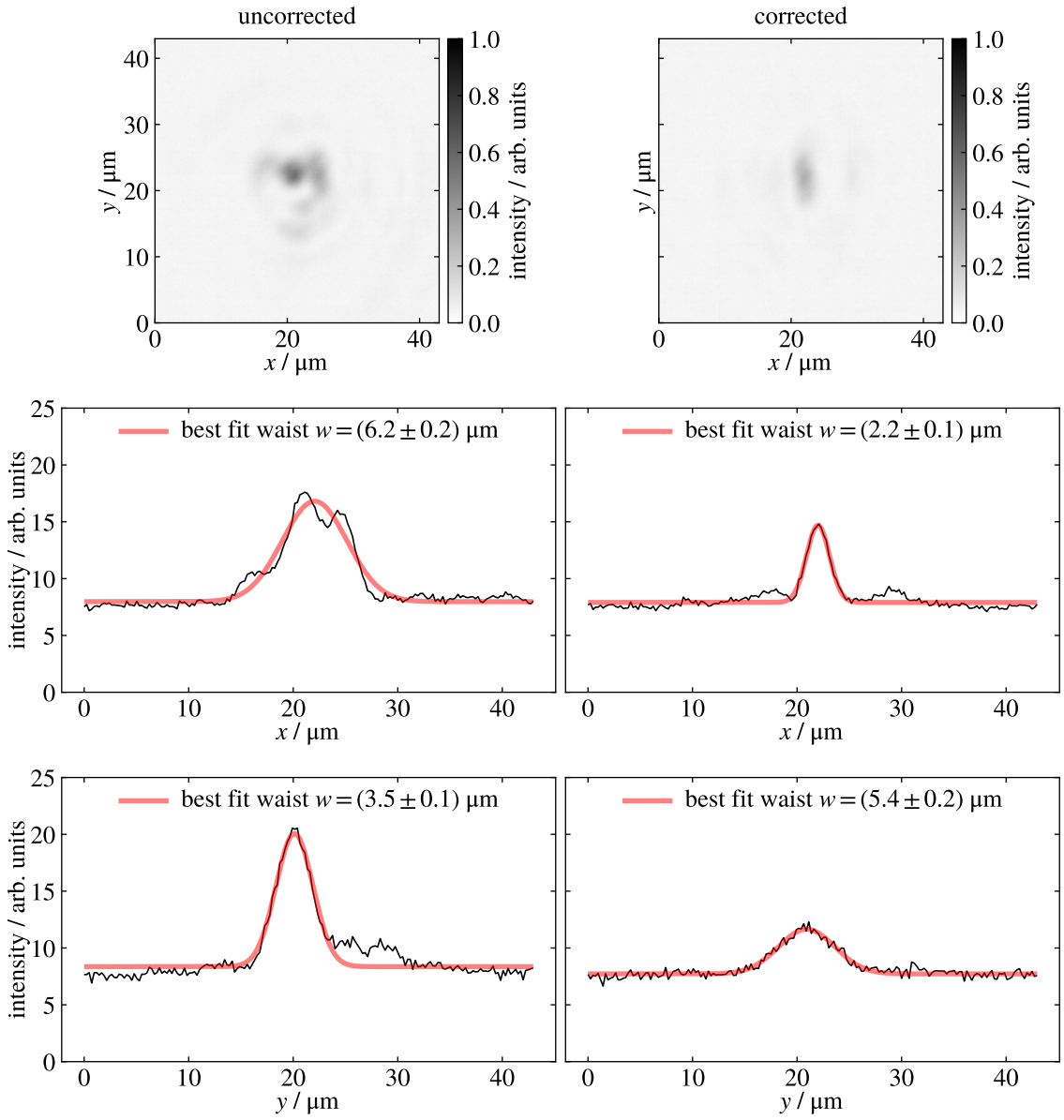

Figure 3.5: Comparison of the spots obtained using the phase pattern without (left) and with (right) aberration corrections. The images were taken using the microscope. The profiles are made by summing perpendicular to the axis along which the profile is taken. Gaussians are fitted to the profiles to determine the beam waists. While the beam waist gets smaller with corrections in the x-direction, the aberration correction pattern has the opposite effect in the y-direction. The shape of the beam does get nicer in both directions when the correction pattern is used, although in the x-direction two stray spots on each side show up.

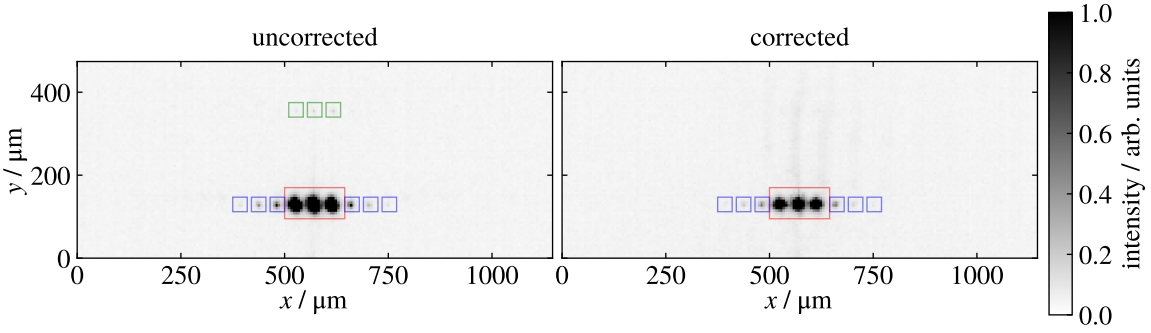

Figure 3.6: These images were taken at a beam power of (9.6±0.1) µW, saturating the main spots but not saturating stray spots and background speckles. The amount of power in stray spots is measured by adding up the powers of the pixels in the marked regions (green: stray spots above, blue: stray spots on the side), the background power is measured by adding up the powers of the remaining pixels. In the uncorrected case, the power in the main spots (marked in red, all three of them added together) is estimated to be (0.60±0.07) µW ((0.32±0.03) µW, values for corrected case in parentheses). The ratio of the powers of the stray spots at the top to the main spots are, from left to right, (0.015±0.004) %, (0.014±0.004) %, and (0.009±0.003) %. The powers of the stray spots to the left and right of the main spots are, again from left to right, (0.011±0.003) %, (0.029±0.003) %, (0.14±0.04) %, (0.14±0.05) %, (0.049±0.003) %, and (0.015±0.003) % ((0.023±0.006) %, (0.035±0.006) %, (0.14±0.07) %, (0.17±0.07) %, (0.052±0.006) %, and (0.023±0.006) %). The total power in the background is (4±2) % ((9±4) %) of the main spots' power.

be expected. This behavior is also seen in the next measurement, which quantifies the background intensity.

3.3.2 Background intensity

Two images are taken with the SLM displaying the same phase pattern, but at different powers of the incident beam, namely (0.032±0.004) µW and (9.6±0.1) µW. The measurement is done with and without the aberration correction pattern (four images in total, the high-power ones are shown in the figure 3.6). The first power is so low that the pixels of the main spots are not saturated, allowing their power to be measured. Since the fraction of the total power diffracted into the main spots should be constant, their powers in the second image can be estimated even though their power cannot be determined directly from the image. The estimate yields (0.60±0.07) µW ((0.32±0.03) µW with aberration correction) for the total power in the traps, which is (6.3±0.7) % ((3.3±0.3) % with aberration correction) of the power of the incident beam. This estimate of the power in the main spots is compared to the total power in the background and to the power in stray spots.

The amount of power in each of the stray spots is below 0.2 % of the total power in the main spots. They should thus not pose a problem.

The total background intensity is (4±2) % of the main spots' power without the aberration correction pattern and ((9±4) %) with it. It does not appear to be very localized. One exception are the streaks that are visible in the image made with the aberration correction pattern. Since their area is quite large, their intensity is still much smaller than that of the main spots.

Just as in the previous measurement, the aberration correction phase pattern does not act as expected:

One would expect the power in stray spots and in the background to be reduced, since fewer optical aberrations should allow better focusing of the beam, but the opposite is the case: The power in the main spots is cut in half, the power in the background is doubled and the power in stray spots is slightly increased too.

3.3.3 Minimal spacing

To measure the minimal possible trap spacing, phase patterns for displaying two spots at varying distances are computed as done before for three spots, again with and without the aberration correction phase pattern. The resulting image is summed perpendicular to the axis along which the spots are laid out to obtain 1D-profiles. A constant background is subtracted.

To determine which of the features in these profiles are unavoidable artifacts of the specific phase pattern used and which are introduced by the imperfect system, the theoretically expected profiles are calculated by using formula 2.4 (see the note in section 2.3.3 about numerical calculations at resolutions larger than the SLM's), and summed the same way as the measured profiles.

The results along with the predictions are shown in figure 3.7. Note that the prediction is scaled such that its maximum matches the measured maximum. The aberration correction pattern is not incorporated into the prediction, since it assumes an ideal system.

For very small separations, the agreement between the prediction and the measurement is better for the corrected version: The distances of the spots match the prediction for small separations instead of just for large ones. The non-evenness of the spots is not predicted. Some stray spots are predicted successfully, namely the ones on the left sides of the spots separated by 20 µm, 30 µm, 40 µm, and 50 µm. Other stray spots are not predicted, especially egregiously the ones to the right of the spots separated by 5 µm, 10 µm, 20 µm, and 30 µm.

One caveat of this setup is that the microscope may introduce aberrations in addition to the ones in front of the first image plane. The latter ones' effects have been corrected in the second set of measurements, but those of the microscope have not.

Again, the peak intensities of the spots made with the corrected patterns are lower, opposite to expectations.

At the minimal separation of 5 µm, the two spots are still clearly separated, but their distance is slightly larger than expected, even with the correction pattern. Without it, the distance between the peaks is much larger than 5 µm. The separation is still fairly close to twice the minimum achievable waist. Smaller separations are not expected to yield distinct spots. Thus, with the aberration correction pattern, spots separated by about twice their waist can be made, at the cost of lower intensity.

3.3.4 Diffraction efficiency

Because of the zeroth-order spot at the center, any intensity pattern has to be displayed off-center. This offset is achieved by adding a grating pattern onto the phase pattern corresponding to the spots that should be created. As stated in section 2.4, the SLM's discrete nature reduces the diffraction efficiency. It is smaller when each grating period consists of fewer levels. This effect limits the maximum power of spots created off-axis. The diffraction efficiency as used here is defined to be the ratio between the diffracted power and the power of the zeroth-order spot when a constant phase is displayed on the SLM.

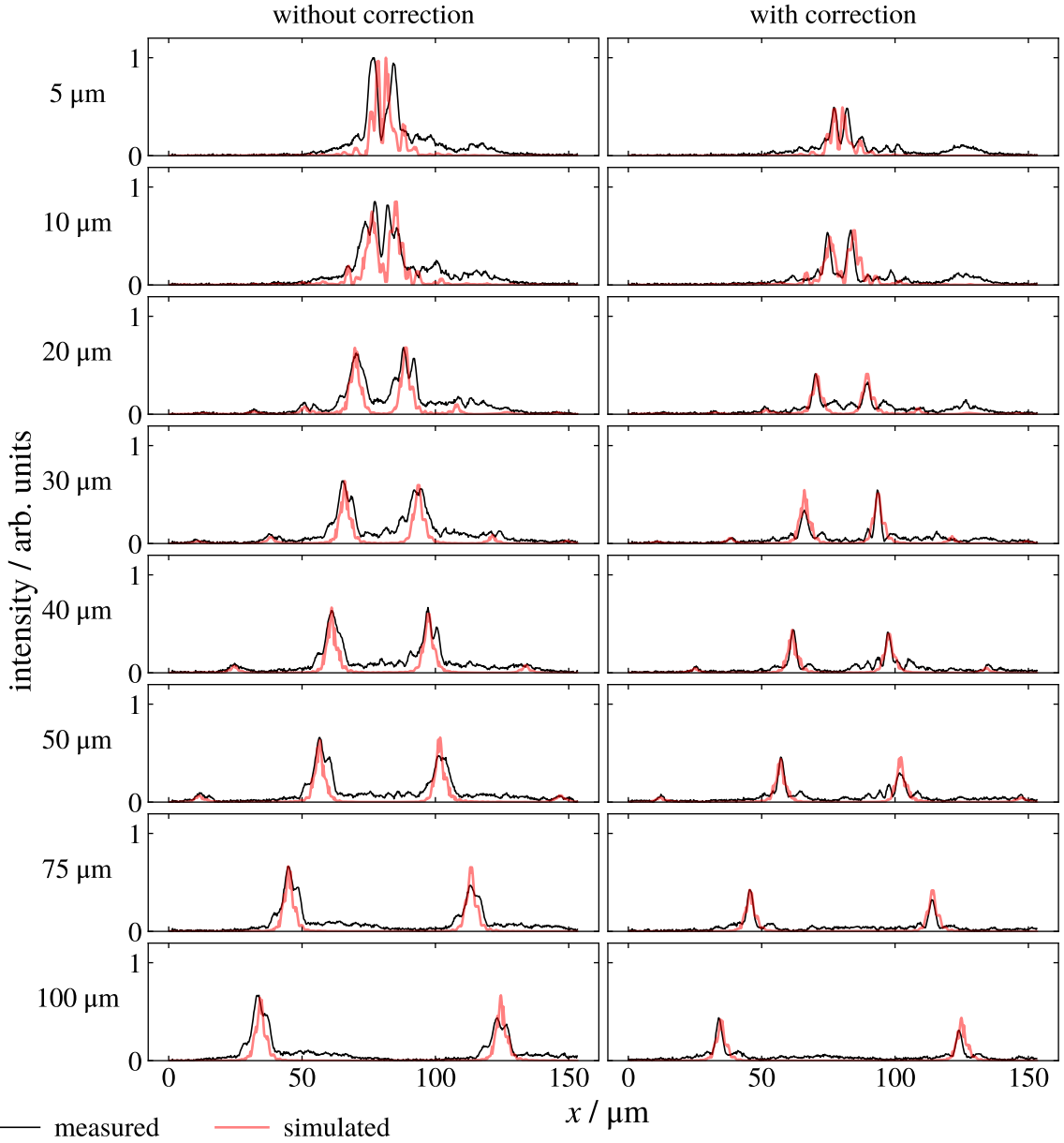

Figure 3.7: The measured intensities (summed in the direction perpendicular to the line between the spots) along with the theoretical prediction made using the exact phase pattern displayed on the SLM are shown. All predictions are scaled by the same factor in the x-direction to compensate for a systematically smaller-than-expected image, and shifted to match the two most prominent peaks to compensate for slight movements of the microscope objective. The intensity of the prediction is scaled to match the maxima. Background intensity has been subtracted for clarity, but would not influence the optical potential for an atom due to being constant.

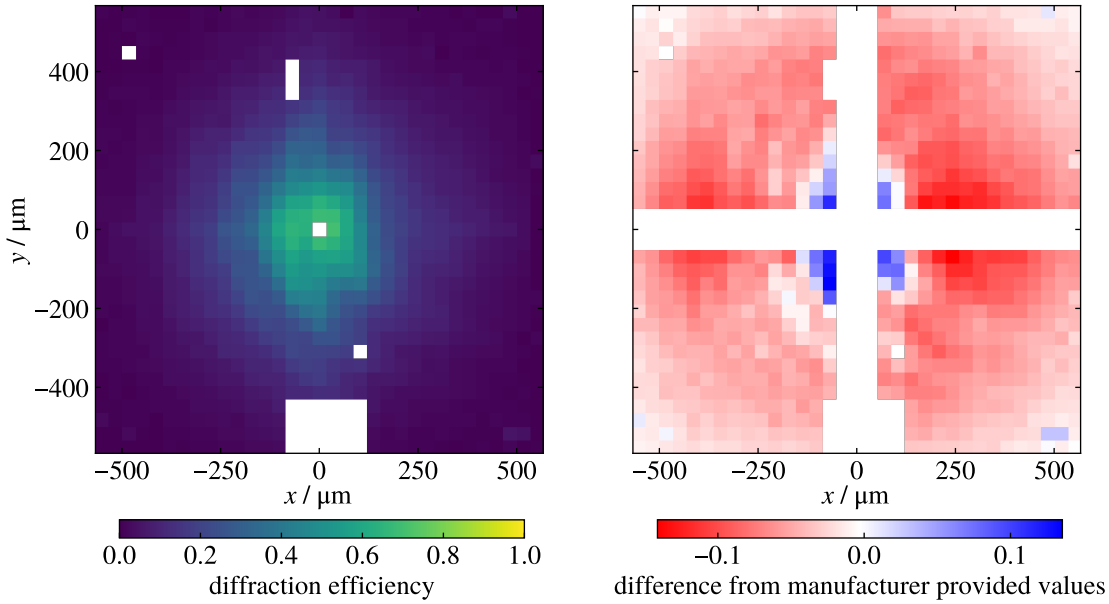

Figure 3.8: On the left, the measured diffraction efficiency, defined as the ratio of the power of a spot to the power of the zeroth order spot while no pattern is displayed, is shown. It is measured by displaying gratings of various frequencies and directions on the SLM. On the right, the measurement is compared to manufacturer provided values for the diffraction efficiency, where available (a negative difference means that manufacturer provided value is larger). Except for the area right around the zeroth order, the diffraction efficiency that was measured is smaller than it should be. White areas indicate missing data.

To measure the diffraction efficiency, diffraction gratings corresponding to shifts to different locations are displayed on the SLM. 33×33 different positions are evaluated. The intensity of a spot is calculated by fitting a 2D-Gaussian with background to the measurement. The results of this are shown in figure 3.8. For some locations, measurements are missing, due to either dead pixels on the camera, being too close to the zeroth order, or a problem with the timing of capturing an image and displaying the phase pattern.

As expected, the diffraction efficiency is largest closest to the zeroth order and gets worse at larger distances. The manufacturer of the SLM provides diffraction efficiencies for spatial frequencies of 5, 10, 20 and 40 line pairs per mm [23]. These values are linearly interpolated and computed for the spatial frequencies displayed on the SLM[4]. Since a shift in the x- and y-direction is accomplished by adding gratings in two directions, the efficiencies corresponding to the two spatial frequencies in each direction are multiplied to obtain the total diffraction efficiency at that point.

The difference between these interpolated manufacturer-provided values and the measured values is also shown in figure 3.8. Because there are no values for shifts corresponding to spatial frequencies smaller than 5 line pairs per mm, there is a cross of missing values in the figure. The measured diffraction efficiency is slightly larger than the manufacturer-provided value at low spatial frequencies but lower at high spatial frequencies. The difference is especially pronounced in two areas to the left and right of the zeroth order. The measured diffraction efficiency is slightly asymmetric, it is higher

[4] The theoretical values obtained from the efficiency of a blazed grating, given e.g. in [24], are not used here because the manufacturer already notes that they are not achieved [23].

for larger shifts in the y- compared to the x-direction. Since the expectation is a symmetric diffraction efficiency profile, this is the reason for the areas with especially large deviations on the x-axis.

The reason for the lower-than-expected diffraction efficiency especially in the x-direction is likely to be the large angle of incidence, since that is the only difference between the two axes. This makes sense, since the large angle of incidence is compensated by stretching the phase pattern in the x-direction, which means that the grating that diffracts the light has fewer periods, and thus worse efficiency. On the other hand, the large angle of incidence decreases the minimal grating period, since the pixel pitch is effectively reduced, allowing light to be diffracted further away from the zeroth order. In essence, the incidence angle stretches the image in the x-direction, and the formerly symmetric diffraction efficiency pattern is stretched with it.

3.3.5 Evaluating the effect of the aberration correction pattern

The aberration correction pattern has both positive and negative effects: Positively, it makes the spots' shapes more Gaussian, and reduces their waist in the x-direction. It also reduces the minimal achievable distance between two neighboring spots, and leads to a closer match between the expected trap spacing and the measured one, for small spacings. On the other hand, it increases the spots' waists in the y-direction. It also cuts the amount of light diffracted into the spots in half and increases the amount of background light by a factor of two.

The negative effects are in disagreement with what one would expect and with the effects e.g. ref. [15] has achieved with the same technique. Because the measured aberrations are much larger than anything applied e.g. in refs. [14, 15], it seems likely that the measurement of the aberrations using the Shack-Hartmann sensor partially mischaracterized the aberrations, due to a non-collimated beam being measured. This seems even more likely given the fact that ref. [15] used a very small focal length lens, which would likely introduce more aberrations than the comparatively large focal length objective used here.

It may be worth trying other approaches for aberration correction. The modified IFTA with projection onto Zernike polynomials from ref. [14, pp. 110ff.] was already tried unsuccessfully, but other possible approaches remain: The beam could be collimated again behind the objective, though this would require another lens of similarly small focal length as the entire system used so far, before measuring the wavefront with the Shack-Hartmann sensor. Another approach is using the SLM itself as a Shack-Hartmann sensor by characterizing the displacement of spots shifted using gratings [14, pp. 123ff.]. All these approaches could also be implemented using rectangular Zernike polynomials, which are the Zernike polynomials re-orthogonalized using the Gram-Schmidt-procedure for a rectangular aperture instead of a circular one. For the Shack-Hartmann sensor wavefront measurement, this has already been tried, but while the measured wavefront could be reproduced well using a linear combination of the rectangular Zernike polynomials, displaying them on the SLM diffracted no light at all into the intended intensity pattern. This also hints at the wavefront measurement being faulty.

3.4 Iterative improvement of spot intensity evenness

When multiple spots are created using the SLM, their powers should be as even as possible, such that when they are later used as dipole traps for atoms, these traps are evenly deep. Remaining aberrations of the optical system, as well as imperfect phase patterns that do not yield perfectly even trapping spots

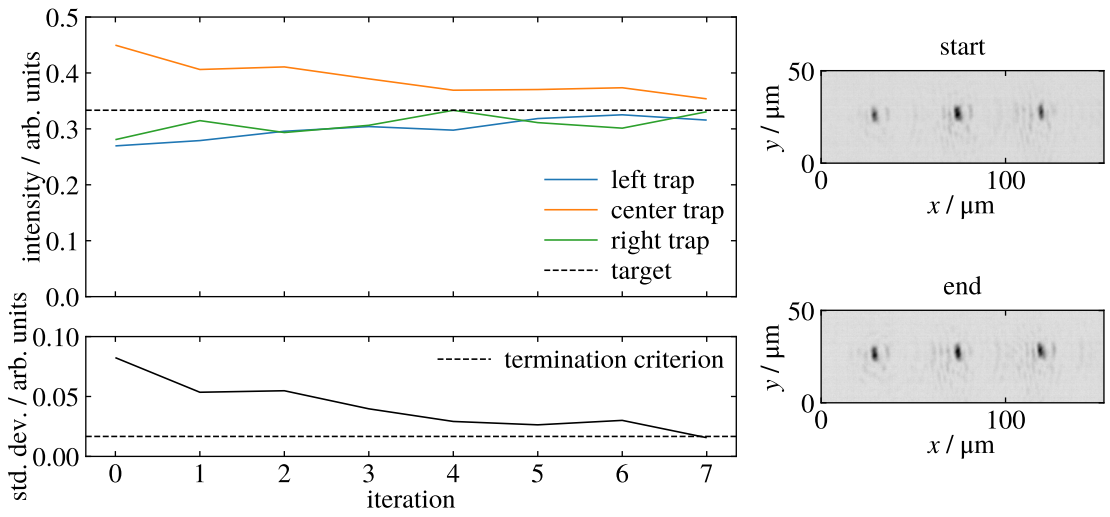

Figure 3.9: In the top left graph, the measured brightness of the three spots is shown for each iteration. The brighter spot is dimmed, and the two darker spots are made brighter. The bottom left graph shows the standard deviation of the three spots' intensities, which is used as a termination criterion for the iterative procedure. The measured pattern at the start and after termination of the procedure are shown on the right. The spots' shapes are maintained, but they look more evenly bright.

even in theory, can cause the power to be distributed unevenly. To compensate, the target intensities of the spots may be adjusted and the phase pattern recomputed.

This is done iteratively using the following procedure, which is the same one as in ref. [15, pp. 59ff]. An initial phase pattern is displayed on the SLM and the spot powers are measured. The target brightness $I^{(i)}_{\text{target}}$ of the spot i is adjusted to

$$I^{(i)}_{\text{target}} + \mu \left(I^{(i)}_{\text{target, initial}} - I^{(i)}_{\text{measured}} \right),$$

where μ is a parameter that is used to adjust the rate of change. Too large changes may lead to overshooting. All intensities are relative, i.e. $\sum_i I^{(i)} = 1$. They are measured by fitting a two-dimensional Gaussian to each spot in each iteration.

An example of this procedure being used to make three spots more even is shown in figure 3.9. In this case, $\mu = 0.2$ was used. One can clearly see that the brightest spot's intensity is lowered and the two dimmer spots' intensities are increased. The standard deviation is used as a measure of intensity evenness. It steadily drops until reaching a value that was chosen as a condition for termination. Quantitatively, the maximum intensity difference between two spots could be reduced from 18 % of the total intensity of the spots to 4 %.

CHAPTER 4

Integration with an existing crossed-beam dipole trap

The Rubidium Quantum Optics (RQO) experiment is used to study Rydberg-states as a way of realizing non-linear interactions between atoms and light at intensities of single photons. For this purpose, ^{87}Rb atoms are trapped and cooled in a magneto-optical trap. The atoms are cooled further, prepared in states of interest, and probed, after being transferred to an optical dipole trap.

The existing experiment already contains a dipole trap consisting of two crossed beams, onto which the smaller dipole traps created with the SLM may be overlaid. As a first step towards implementing smaller dipole traps in addition to the existing crossed-beam dipole trap in the experiment, the laser that will be used for them is set up with optics for polarization and intensity stabilization as well as intensity adjustment; this is described in section 4.1. The same laser was used for characterizing the SLM in the previous chapter. In order to determine whether the intensity distribution created with the SLM is suitable for its intended purpose, the intensity is measured outside the focal plane and compared to simulations (section 4.2). From the results, the trapping potential and atomic distribution are computed, and compared to those of the previously used three-beam dimple trap (section 4.3). Finally, an approach for moving the focal plane of the SLM easily, which might be necessary for alignment, is evaluated (section 4.5).

4.1 Laser setup

The SLM requires horizontally linearly polarized light when used at a non-zero angle of incidence [23], so it is important that the light's polarization does not change over time.

The setup of the laser is shown in figure 4.1, including some parts that are only needed for alignment once. The laser beam polarization is cleaned up using a PBS, which is also used to dump a large portion of the laser's power, since the camera that is used to measure the intensity pattern saturates at a few µW, but the output power of the laser used (Toptica TApro at 805 nm) is hundreds of mW. If the SLM is used to trap atoms, these higher powers will be utilized. A telescope is used to improve the beam's shape such that it is more easily coupled into a polarization maintaining single-mode fiber. An AOM is introduced to allow stabilizing the beam's intensity and switching the beam on and off, which will be required later in the experiment. The PBS behind the AOM makes it possible to use a portion of the laser power for other purposes, for example the AOD-part of a possible future combined

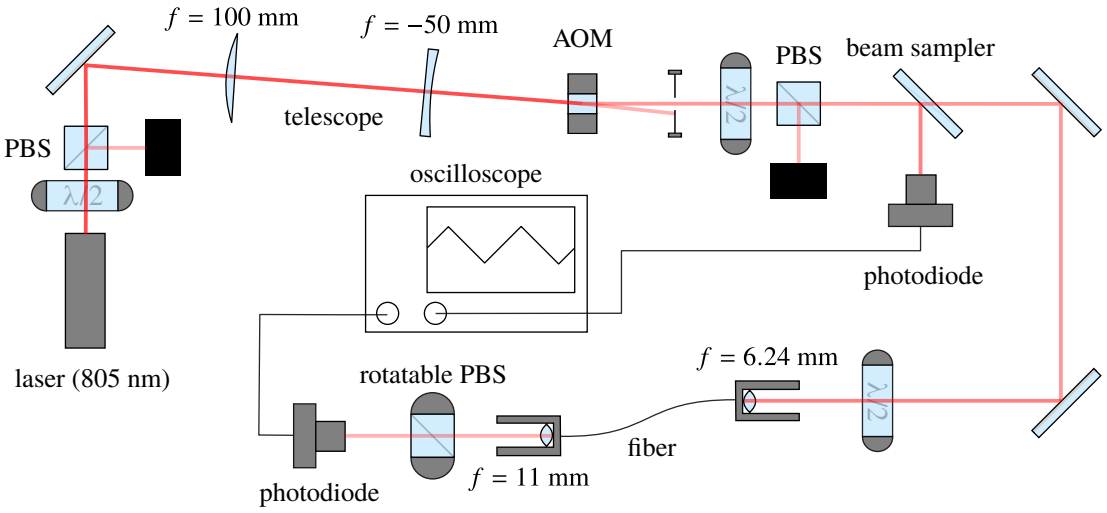

Figure 4.1: On the laser table, the beam of the 805 nm diode laser TApro805 is cleaned in polarization using a PBS, which is also used to reduce the beam's power. The beam, which is elongated, is reshaped using a telescope, and sent through an AOM, which modulates the intensity of its first diffraction order, the zeroth order is dumped. Another waveplate and PBS are inserted to split the laser power for a future additional AOD-trap. Some of the light is diverted using a beam sampler into a photodiode. Two movable mirrors are used to couple the beam into a fiber. Right in front of the fiber, a waveplate is placed to match the polarization axis of the linearly polarized light with the polarization maintaining fiber's axis. On the other table, the light is sent through a rotatable PBS and then onto a photodiode. The photodiodes, beam sampler and oscilloscope are only necessary for aligning the polarization axis of the light at the input with the polarization maintaining fiber's axis.

SLM and AOD dipole-trap. To ensure that the linear polarization is maintained at the other end of the polarization maintaining fiber, which is not rotationally symmetric, it must be aligned with the polarization axis of the light.

To do this alignment precisely, the following effect is used. The polarization maintaining fiber has two axes with different refractive indices n_1 and n_2. When the input light's polarization axis is not aligned with one of these axes, the portion of the light polarized along axis 1 propagates with refractive index n_1, and the portion polarized along axis 2 propagates with refractive index n_2. This leads to a phase shift between these two components of the light, and thus to in general non-linearly polarized light at the output. This phase shift, and thus the polarization state at the output, depends on the light's frequency. The frequency is varied by scanning the laser frequency by applying a linear ramp to the laser piezo voltage.

A PBS at the output is used to analyze what part of the light is linearly polarized in a certain direction. Because the laser intensity varies when the frequency is being scanned, the signal of the photodiode used to measure the PBS output intensity is divided by the signal of a photodiode that measures the laser's intensity before any polarization optics. The optimization procedure is the following: The rotatable PBS on the output side is rotated such that the relative signal's variation is maximal. This is equivalent to finding the axis that is most sensitive to polarization changes in the fiber. The input polarization axis is rotated such that this variation is minimized (i.e. the input polarization alignment is improved). Then, a different axis where the ratio of light polarized in that direction varies maximally is found. These steps are repeated until the amount of light polarized along

any axis varies very little. At that point, the fiber's axis is well matched with the polarization axis.

After performing the alignment, the ratio between the beam's maximum and minimum power behind a rotatable PBS behind the fiber was 2 300, indicating a very cleanly linearly polarized beam.

The laser set up in this section will be used for the dipole traps created with both the SLM and the AOD. The latter requires a second identical beam path at the other output of the power-splitting PBS, which has not been set up yet. Using this laser for the characterization of the SLM ensures that the results are applicable to its integration with the RQO-experiment.

4.2 Intensity outside the focal plane

To obtain a three dimensional trapping potential, the intensity distribution outside the focal plane must be known. The intensity may be measured there by moving the microscope and camera through the focal plane on a translation stage. Numerically, the intensity may be obtained using the angular spectrum method described in ref. [13, pp. 55ff.], which will be briefly summarized.

The angular spectrum of the field $U(x, y, z)$ in a plane at position z is defined as its Fourier transform in the plane $A(\xi, \eta, z) = \mathcal{F}_{x,y}[U(x, y, z)](\xi, \eta, z)$ (the notation $\mathcal{F}_{x,y}$ is supposed to indicate that only x and y are considered as variables to be Fourier transformed). The field is thus given by the inverse Fourier transform of the angular spectrum, $U(x, y, z) = \mathcal{F}^{-1}_{\xi,\eta}[A(\xi, \eta, z)](x, y, z)$. Inserting the field in that form into the Helmholtz equation 2.1 yields $\frac{\mathrm{d}^2 A}{\mathrm{d}z^2} + 2\pi\sqrt{1/\lambda^2 - \xi^2 - \eta^2}A(\xi, \eta, z) = 0$, with the solution $A(\xi, \eta, z) = A(\xi, \eta, 0)e^{2\pi i\sqrt{1/\lambda^2-\xi^2-\eta^2}}$. The case of $(\xi\lambda)^2 + (\eta\lambda)^2 > 1$ corresponds to evanescent waves, which only occur in cases where the assumptions underlying the scalar wave theory cease to hold [13, p. 58]. The propagation of the angular spectrum is thus simply done by multiplication with a phase factor, and the field is propagated by Fourier transforming the input field to obtain the angular spectrum, propagating the angular spectrum, and finally inverse Fourier transforming the angular spectrum at the plane of interest to find the field there.

This method of field propagation is implemented in the Python library diffractsim [25], which is used to numerically do this propagation and obtain the intensity outside the focal plane. The library allows easy calculation of parts of a propagated plane at a higher resolution by implementing the method described in ref. [26], which significantly speeds up the 3D-intensity calculation, since only an area that is small compared to the SLM is required for the trapping potentials.

Measuring the intensity outside the focal plane

The prediction of the angular spectrum method is tested against measurements of the intensity outside the focal plane. The region that will be interesting for the optical potential for the atoms is approximately 110 µm thick, which is twice the waist of the beams forming the crossed beam dipole trap. The following measurements are partially taken at distances from the focal plane which are larger than 55 µm, but will still allow evaluating whether the propagation method actually produces intensities at planes outside the focus that match the experimentally measured intensities. For intensity patterns that only contain spots, the intensity close to the focal plane should be similar to that of Gaussian beams. Whether this is the case is also evaluated. The results of performing measurements around the focal plane are shown in figure 4.2, with the expected intensity obtained both via propagation of the field created by the SLM to non-focal planes and via Gaussian beams with foci in the focal plane.

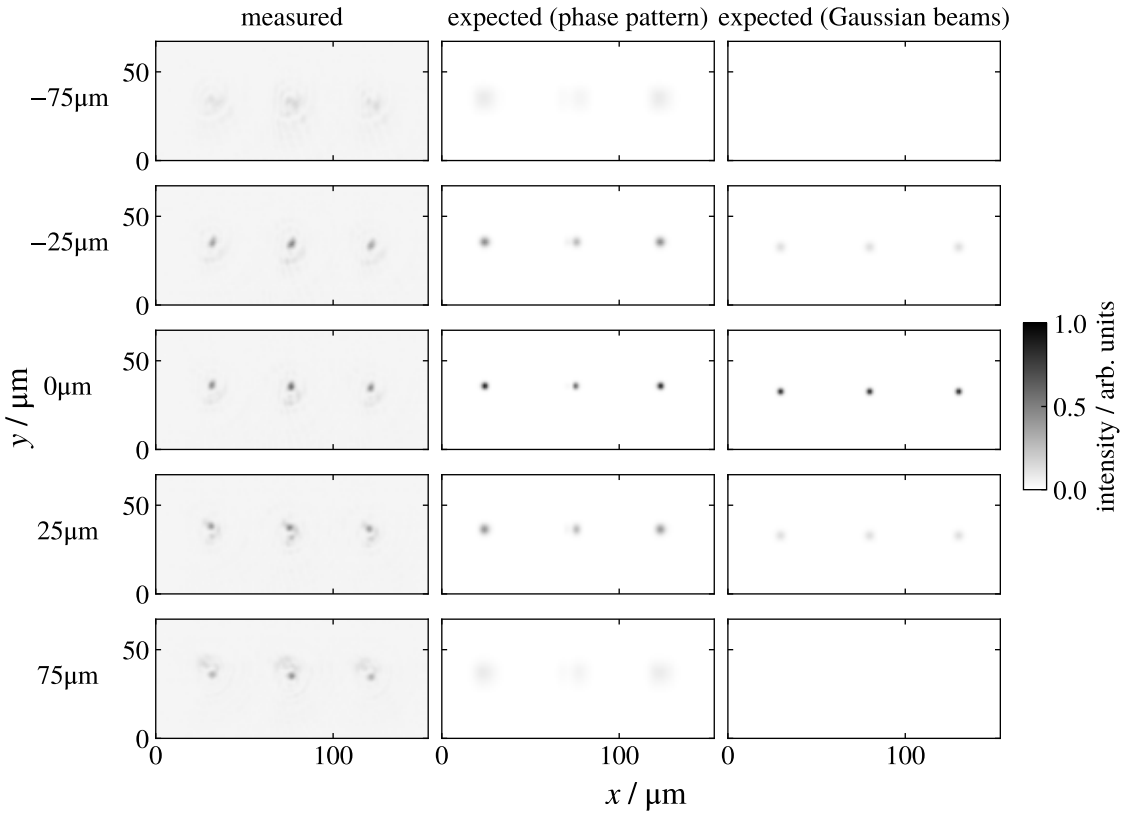

Figure 4.2: In the left column, the intensity measured at different distances from the focal plane is shown. The expected intensity in these planes is shown in the middle and right columns, obtained once by propagating the field created by the SLM and once by propagating the target intensity in both directions, which consists of Gaussian beams.

The rings of stray intensity around the spots in the focal plane are also visible outside of it. Toward the SLM, the spots diverge at a similar rate as predicted. In the other direction, a tightly focused spot in the middle remains further away from the focal plane than expected. The propagated SLM-field leads to spots that diverge less quickly than ideal Gaussian beams would, which is closer to the measured behavior.

It is not clear whether the ring-patterns around the spots are an artifact of using the microscope to image the spots, since they are too small to be visible without the microscope. Because of the crossed dipole trap's limited radial size, the differences of the measured intensity outside the focal plane from a diverging Gaussian beam are unlikely to cause unwanted trapping potentials.

For phase patterns made just of spots, the easier description with just propagated Gaussian beams is likely to be sufficient for any calculations requiring the trapping potential. The full propagation method might be useful for more intricate intensity patterns.

4.3 Trapping potential for ^{87}Rb in an optical dipole trap

Given the intensity distribution calculated and measured in the previous section 4.2, the trapping potential and atomic distribution may be calculated.

The RQO-experiment uses ^{87}Rb. The trapping potential in an optical dipole trap is given by the light shift of the state of interest. In this case, the intention is to trap atoms in the ground state. For an alkali atom with nuclear spin $I = 3/2$, such as ^{87}Rb, the potential is therefore [7, eq. 19]

$$U(\vec{r}) \approx \frac{\pi c^2 \Gamma}{2\omega_0^3} \left(\frac{2}{\Delta_2} + \frac{1}{\Delta_1} \right) I(\vec{r}),$$

where ω_0 is the resonance frequency of the D1 and D2 transitions, Γ is the decay rate of the excited states, Δ_1 and Δ_2 are the detunings of the laser frequency from the D1- and D2-lines respectively, and $I(\vec{r})$ is the intensity of the light at the position $\vec{r}$. Since the resonance frequencies of the D1- and D2-transitions differ only by 2 %, and the line widths of the $5P_{1/2}$ and $5P_{3/2}$ states differ only by 5 %, the resonance frequency of the D2 transition is used for ω_0 and the linewidth of the $5P_{3/2}$ state is used for Γ.

For a given number N of atoms at a temperature T that are trapped in the potential, their spatial distribution is given by the Boltzmann distribution [7, eq. 32]

$$n(\vec{r}) = n_0 \exp\left(\frac{U(\vec{r})}{k_B T} \right),$$

with n_0 chosen such that $\iiint n(\vec{r})\, \mathrm{d}V = N$.

In the experiment, the density of atoms is measured via absorption imaging and indirectly via the absorption of a probe beam. As a measure for the density of the atoms, the optical depth (OD) is used. It is defined as $\sigma_0 n_c / (1 + \delta^2)$. The resonant cross section for absorption is $\sigma_0 = 6\pi\lambda^2$ for a two-level atom. The probe laser at 780 nm excites the D2 transition, so its wavelength is used for λ. n_c is the column density of the cloud, i.e. $n_c(x, y) = \int n\, \mathrm{d}z$, where z is the direction of the probe beam, and $\delta = \frac{\omega - \omega_0}{\Gamma/2}$ is the detuning of the probe beam's frequency ω from the resonant frequency of the atoms ω_0. [27, p. 23]

For a probe beam with a non-zero waist, each column is weighted by the intensity of the beam there, such that the optical density is then given by

$$\mathrm{OD} = \iiint n(\vec{r}) \sigma_0 \frac{I_{\mathrm{probe}}}{P_{\mathrm{probe}}}\, \mathrm{d}V$$

when the detuning of the probe beam is zero. In the next section, the OD will be used to compare the SLM- and AOD-generated traps.

4.4 Simulation of trapping potentials

In this section, the trapping potential of the intensity pattern created with the SLM is compared with the trapping potential that has been created using an AOD before, as described in ref. [11], and with that of the existing crossed-beam trap. The crossed-beam trap consists of two Gaussian beams with

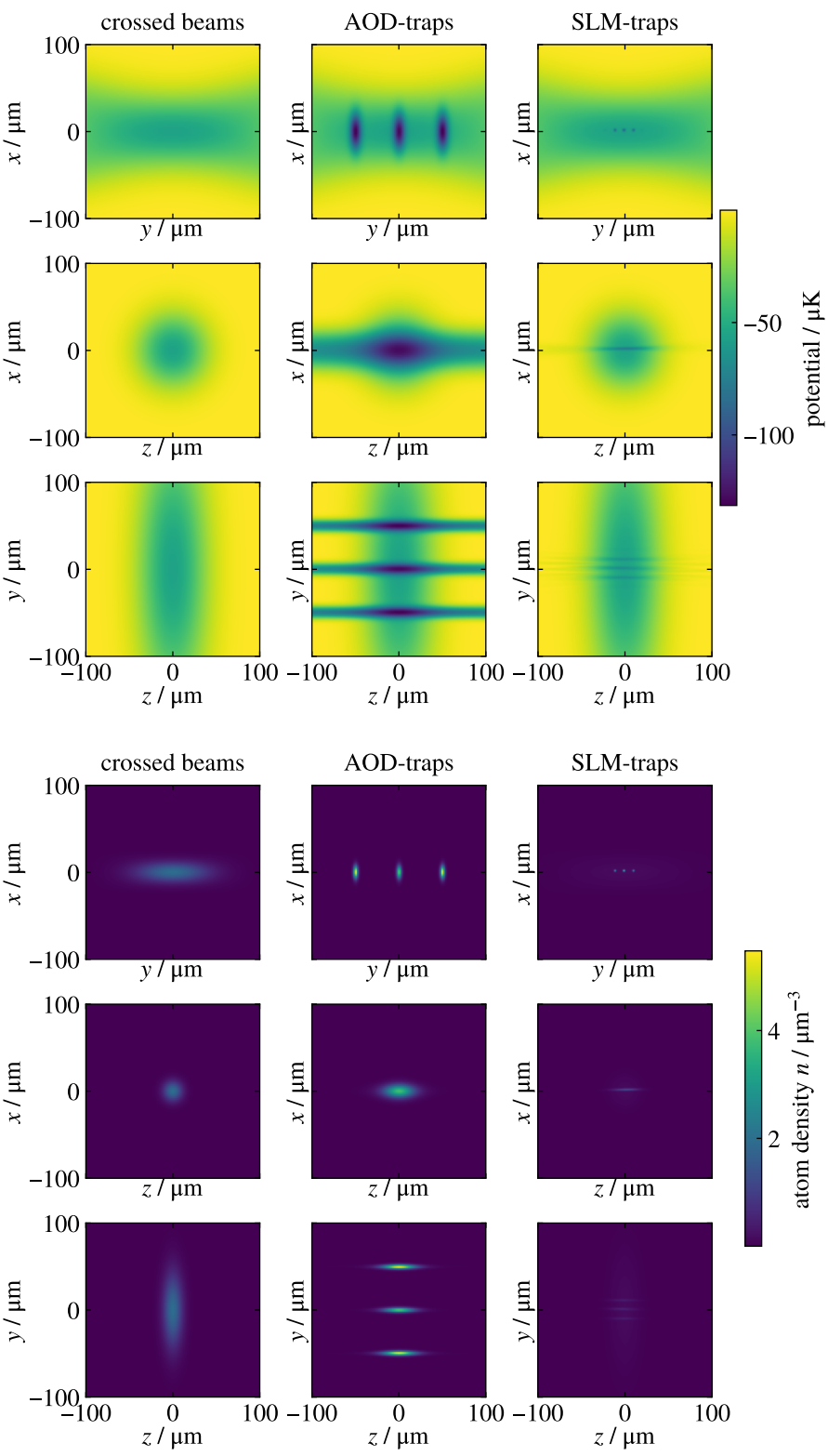

Figure 4.3: In the top figure, the simulated potentials for three traps are shown: Just the crossed-beam dipole trap on the left, the crossed-beams with additional AOD dimple-traps in the middle, and with additional SLM-traps on the right. Three slices through the origin are shown: The xy-plane in the top row, the xz-plane in the middle and the yz-plane in the bottom row. In the bottom figure, the corresponding atom distributions are shown. The crossed beams propagate at a 15° angle from the y-axis. The SLM- and AOD-beams propagate along the z-direction. The wavelength of the crossed beams is 1 064 nm, that of the AOD- and SLM-beams is 805 nm. The crossed beams each have a power of 1 W, the dimples have a total power of 60 mW, and the SLM is simulated as being illuminated by a 10 mW beam. The large loss of light, measured to be 94 % in section 3.3.2 is taken into account. The intensities of the individual beams created by the AOD and SLM are adjusted to obtain similar atom densities in all three traps. The total number of atoms is $6{\times}10^4$ for the crossed beams and $3{\times}10^4$ for the other two traps. Their temperature is 10 µK.

wavelength 1 064 nm and waists of 55 µm intersecting at a 30° angle. They propagate at angles of 15° to the y-axis. The intensity distribution created using the AOD, that is overlaid onto the crossed beams, consists of three elliptical Gaussian beams with wavelength 805 nm and waists of 9 µm in the y- and 29 µm in the x-direction. The SLM-traps are similar to the ones characterized in chapter 3, i.e. three spots with wavelength 805 nm focused as tightly as possible with a distance between them of 10 µm. The exact intensity distribution is calculated as described in section 4.2, i.e. from the phase pattern displayed on the SLM.

In the simulation, the temperature of the atoms is chosen to be 10 µK, which is what has been measured in previous experimental iterations using absorption imaging [11]. The number of atoms is chosen to be 6×10^4 for the crossed-beam trap and 3×10^4 for the AOD- and SLM-traps, since loading these traps causes some atom loss. The power of the crossed beams is 1 W each, the dimple traps have a power of 60 mW in total, and the SLM is simulated to be illuminated with a 2.2 mm waist Gaussian beam with a power of 10 mW. The large power loss of 94 % measured in section 3.3.2 is accounted for.

In figure 4.3, the trapping potentials resulting from the three different intensity distributions and corresponding atomic distributions are shown. The optical depth is calculated as a measure of the density of the atoms that can be compared to what has actually been achieved in the experiment.

It is clearly visible in figure 4.3 that the density of the atom cloud is increased with the additional dipole traps. This would be reflected in a higher optical depth, but atom loss causes it to be lower. For the crossed-beam trap, an optical depth of 34 is calculated, for the AOD-traps 14 and for the SLM-traps 5.5. If the number of atoms stayed the same, the optical depth for the two extra dipole-traps would be higher due to more atoms being in a region where the probe beam's intensity is higher (at 6×10^4 atoms 29 for the AOD-traps and 11 for the SLM-traps). The SLM-traps do not have higher OD than the AOD-traps even though they are much smaller because they are not deep enough to trap all atoms, and some atoms stay in the outer crossed-beam trap. This could be avoided by increasing the intensity of the beam. At a power of 20 mW, the SLM traps' OD would be 18.

The SLM-traps that were simulated in this section were chosen as similar as possible to the ones characterized in chapter 3. They are thus a lot smaller than the AOD-traps, and figure 4.3 clearly shows that the atoms are not completely confined to the traps. This might be remedied by using a loading scheme such as the one used for the AOD-traps; the crossed-beam trap was briefly turned off in the experiment using them to ensure that no atoms remain outside of them [11]. However, the number of atoms confined in the very small SLM-traps would likely be a lot smaller than in the AOD-traps (the OD values discussed in the previous paragraph provide evidence for this) , which is disadvantageous for their use as Rydberg superatoms. The SLM-traps that have been created in this thesis are therefore likely to be unsuitable for replacing the AOD-traps.

In principle, the SLM permits creating arbitrary intensity patterns, but creating larger spots whose shape is approximately Gaussian and which do not suffer from dark speckles has proven to be difficult. In this thesis, only intensity patterns consisting of many small spots have been created successfully, but this limitation is specific to the optical system and phase retrieval algorithms employed in this thesis; it is possible to create large scale smooth patterns using different phase retrieval algorithms, as demonstrated in refs. [14, 16].

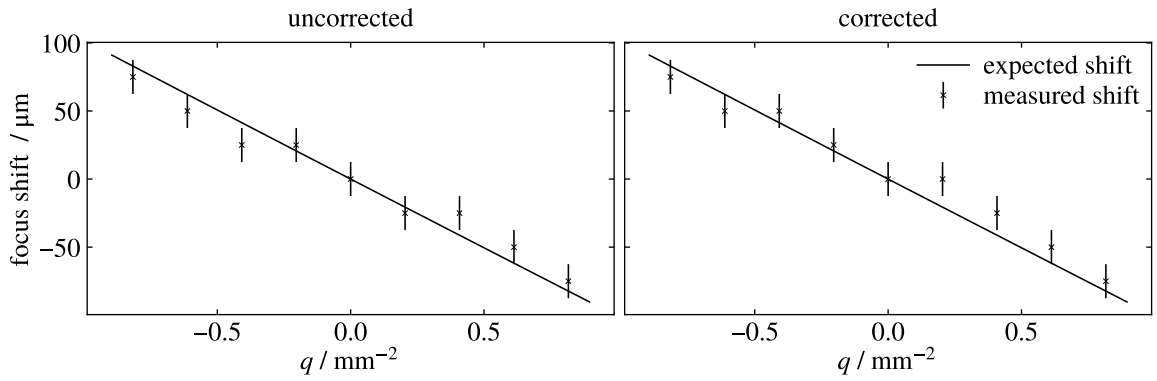

Figure 4.4: Measured shift of the focal plane when displaying a quadratic phase pattern $\phi(x, y) = q(x^2 + y^2)$ on the SLM. The quadratic phase pattern was added to a phase pattern creating three spots, both with and without the aberration correction phase pattern. The shift of the focal plane was measured by determining the plane where the spots' intensities were highest compared to neighboring planes. The errors are half the distance between two neighboring imaged planes. The lines are not fitted, but the expected shifts computed from the displayed phase pattern and the focal length of the glass lens.

4.5 Moving the focus using quadratic phase patterns

For the SLM-traps to work as simulated in section 4.3, it is necessary to align them with the crossed-beam trap in the z-direction. A convenient method for helping with that is presented and evaluated in this section.

As noted in section 2.1, a lens of focal length f imposes a phase $e^{-\frac{ik}{2f}(x^2+y^2)} = e^{iq(x^2+y^2)}$ onto the field. Instead of inserting a physical lens into the beam, this phase pattern may be displayed on the SLM[1]. This second SLM-lens may be used to shift the focal plane in which the image appears, without having to manually adjust the setup. The expected shift of the focal plane for an SLM-lens of focal length f_2 is $\frac{1}{1/f_1+1/f_2} - f_1$, where f_1 is the focal length of the other lens.

A quadratic phase pattern corresponding to lenses of different focal lengths f is displayed on the SLM, in addition to the three-spot phase pattern. For each focal length, the imaging plane is moved through the approximate focal plane using a translation stage in steps of 25 µm, and the location of the focal plane is determined as the one where the peak intensity of the profile obtained by summing perpendicular to the axis along which the traps are laid out is maximal. The errors on the focal position are half the step-size, i.e. 12.5 µm.

The results along with the expectations are shown in figure 4.4. Overall, the shift is as expected. Some larger than expected differences might be due to the quadratic phase pattern being displayed on the SLM being asymmetric, which was only noticed after the measurement. The error was made because the SLM's non-equal side lengths were accidentally ignored. An asymmetric quadratic phase pattern leads to different focal lengths in the x- and y-directions. This measurement is compared to the expected shift in the x-direction, since the intensity maxima were also determined along this axis.

Even though a slightly wrong phase pattern was displayed, the movement of the focal plane agrees well with the prediction, and this method is likely to be useful when aligning the foci of the traps with the focal plane.

[1] It is even possible to completely replace all glass lenses in the system with such a phase pattern (see ref. [17]).

CHAPTER 5

Conclusion and outlook

In this thesis, first steps were taken towards implementing tailored optical potentials with an SLM for use in the RQO experiment.

The Gerchberg-Saxton algorithm for phase-retrieval was implemented. A testing setup was built and its optical aberrations were measured with a wavefront sensor. An intensity pattern consisting of three tightly focused spots was used to characterize the SLM. The smallest achieved spot waist was (2.2±0.1) µm in one direction with aberration corrections, which is the theoretical limit of the optics used. It should be noted that the waist was larger in the other direction. The efficiency of the SLM, i.e. the portion of the input power diffracted into the spots, was measured to be (6.3±0.7) % at most. The background intensity was (4±2) % of the power in the main spots. The intensity in each stray spot was less than 0.2 % of the power in the main spots. The smallest distance between two separate spots that was achieved was 5 µm. The diffraction efficiency of the SLM was measured, it was mostly as expected; differences from the expectation could be explained with the large angle of incidence used. By iterative improvement, the maximum intensity difference between two spots could be reduced from 18 % of the total intensity of the spots to 4 %.

The phase pattern used to correct for aberrations of the optical system led to mixed results. It improved the shape of spots partially and allowed more accurate and smaller spacings between spots to be achieved, but it also lowered the efficiency from (6.3±0.7) % to (3.3±0.3) %, doubled the background intensity and increased the relative brightness of stray spots. This suggests that the intensity patterns could be improved further by better correcting for aberrations. There are different approaches for doing this. One possibility is using the SLM itself in a Shack-Hartmann sensor like configuration, as described in ref. [14]. A brute force search for Zernike coefficients leading to an improvement of the intensity pattern might also be viable, since the search space is not huge and the rate at which images are taken can likely be improved beyond the current 1 Hz, though some work on reliability is needed, as became evident in a few missing datapoints in section 3.3.4. Further improvements may be obtained when using Zernike polynomials for a rectangular aperture instead of for circular ones. It might also be worth revisiting the IFTA-based aberration determination method described by ref. [14].

A laser setup that will be used to implement SLM- and AOD-traps in the RQO-experiment was built. The simulation of the trapping potentials and atom distributions that would be expected for the SLM-traps as characterized showed that they are, at their current small size, unsuitable for replacing the formerly used AOD-traps in experiments with a few Rydberg superatoms. The capability of

shifting the focal plane using the SLM was tested successfully.

To replace the AOD-traps in the RQO-experiment, further work is needed. It is likely that for smooth intensity patterns which are not just made of tightly focused spots, an IFTA-variant called MRAF [19] or the adaptation described in ref. [16] would yield better results. It might be necessary to compromise between very small features and smooth large features, e.g. by removing the second telescope used to create smaller spots from the optical setup.

An almost certain improvement of the image quality could be obtained by reducing the angle of incidence of light with the SLM. The effects of the large angle were noticed in multiple measurements; reducing it is certainly beneficial. Better results at a non-zero angle of incidence might be obtained by using non-quadratic target images instead of stretching the phase pattern, to avoid interpolation effects.

The combination of the SLM with AOD-created dynamic potentials might also be worth looking into, this approach has been adopted e.g. in recent quantum computing experiments with neutral atoms [28, 29].

APPENDIX A

Appendix

n	m	polynomial in cartesian coordinates
0	0	1
1	−1	x
1	1	y
2	−2	$2xy$
2	0	$2x^2 + 2y^2 - 1$
2	2	$-x^2 + y^2$
3	−3	$-x^3 + 3xy^2$
3	−1	$3x^3 + 3xy^2 - 2x$
3	1	$3x^2y + 3y^3 - 2y$
3	3	$-3x^2y + y^3$
4	−4	$-4x^3y + 4xy^3$
4	−2	$8x^3y + 8xy^3 - 6xy$
4	0	$6x^4 + 12x^2y^2 - 6x^2 + 6y^4 - 6y^2 + 1$
4	2	$-x^2 + 4y^4 - 3y^2$
4	4	$x^4 - 6x^2y^2 + y^4$

Table A.1: Table of the first Zernike polynomials with their indices. The polynomials are taken from [30], with the slightly different indexing scheme as used by the software included with the wavefront sensor used.

Bibliography

[1] T. H. Maiman et al., *Stimulated optical radiation in ruby*, Nature **187** (1960) 493, URL: https://www.nature.com/articles/187493a0.pdf.

[2] E. L. Raab, M. Prentiss, A. Cable, S. Chu and D. E. Pritchard, *Trapping of Neutral Sodium Atoms with Radiation Pressure*, Phys. Rev. Lett. **59** (23 1987) 2631.

[3] S. Chu, J. E. Bjorkholm, A. Ashkin and A. Cable, *Experimental Observation of Optically Trapped Atoms*, Phys. Rev. Lett. **57** (3 1986) 314.

[4] D. Frese et al., *Single Atoms in an Optical Dipole Trap: Towards a Deterministic Source of Cold Atoms*, Phys. Rev. Lett. **85** (18 2000) 3777.

[5] N. Schlosser, G. Reymond, I. Protsenko and P. Grangier, *Sub-poissonian loading of single atoms in a microscopic dipole trap*, Nature **411** (2001) 1024.

[6] A. Ashkin, J. M. Dziedzic, J. E. Bjorkholm and S. Chu, *Observation of a single-beam gradient force optical trap for dielectric particles*, Optics letters **11** (1986) 288.

[7] R. Grimm, M. Weidemuller and Y. Ovchinnikov, *Optical dipole traps for neutral atoms*, Adv. in Atomic, Molec., and Opt. Phys. **42** (2000) 95.

[8] G. Gauthier et al., "Dynamic high-resolution optical trapping of ultracold atoms", *Advances in Atomic, Molecular, and Optical Physics*, vol. 70, Elsevier, 2021 1.

[9] T. Peyronel et al., *Quantum nonlinear optics with single photons enabled by strongly interacting atoms*, Nature **488** (2012) 57.

[10] O. Firstenberg, C. S. Adams and S. Hofferberth, *Nonlinear quantum optics mediated by Rydberg interactions*, Journal of Physics B: Atomic, Molecular and Optical Physics **49** (2016) 152003.

[11] N. Stiesdal et al., *Controlled multi-photon subtraction with cascaded Rydberg superatoms as single-photon absorbers*, Nature Communications **12** (2021) 1.

[12] N. Stiesdal, *Collective atom-light interactions with Rydberg superatoms*, PhD thesis: University of Southern Denmark, 2022.

[13] J. W. Goodman, *Introduction to Fourier Optics*, 3rd ed., Englewood, Colorado: Roberts & Company, 2005.

[14] R. van Bijnen, *Quantum Engineering with Ultracold Atoms*, PhD thesis: Eindhoven University of Technology, 2013.

[15] H. Labuhn,
Rydberg excitation dynamics and correlations in arbitrary 2D arrays of single atoms,
PhD thesis: Université Paris-Saclay, 2016.

[16] W. Zhou-Hanf,
Robust Holographic Generation of Arbitrary Light Patterns: Method and Implementation,
Master thesis: Rheinische Friedrich-Wilhelms-Universität Bonn, 2018.

[17] T. Legrand,
Vergleich der Holografie und der direkten Abbildung mit dem räumlichen Lichtmodulator,
Bachelor Thesis: Rheinische Friedrich-Wilhelms-Universität Bonn, 2019.

[18] R. W. Gerchberg and W. O. Saxton, *A Practical Algorithm for the Determination of Phase from Image and Diffraction Plane Pictures*, Optik **35** (1972) 237.

[19] M. Pasienski and B. DeMarco,
A high-accuracy algorithm for designing arbitrary holographic atom traps,
Optics express **16** (2008) 2176.

[20] C. Lingel, T. Haist and W. Osten, *Optimizing the diffraction efficiency of SLM-based holography with respect to the fringing field effect*, Appl. Opt. **52** (2013) 6877.

[21] *USAF 1951 Glass Slide Resolution Targets, Technical Information*,
URL: https://www.edmundoptics.com/f/1951-usaf-glass-slide-resolution-targets/12064/ (visited on 15/08/2022).

[22] D. Meschede, *Optik, Licht und Laser*, Vieweg und Teubner, 2008.

[23] *LCOS-SLM Operation Manual, X10468 Series. X13267 Series. X13138 Series.*
Hamamatsu, 2018.

[24] G. Swanson, *Binary Optics Technology: Theoretical Limits on the Diffraction Efficiency of Multilevel Diffractive Optical Elements*, tech. rep.,
Lincoln Laboratory, Massachusetts Institute of Technology, 1991.

[25] R. de la Fuente,
Diffractsim: A diffraction simulator for exploring and visualizing physical optics,
URL: https://github.com/rafael-fuente/diffractsim.

[26] Y. Hu et al., *Efficient full-path optical calculation of scalar and vector diffraction using the Bluestein method*, Light Sci Appl **9** (2020).

[27] W. Ketterle, D. S. Durfee and D. M. Stamper-Kurn,
Making, probing and understanding Bose-Einstein condensates, 1999,
URL: https://arxiv.org/abs/cond-mat/9904034.

[28] S. Ebadi et al., *Quantum phases of matter on a 256-atom programmable quantum simulator*, Nature **595** (2021) 227.

[29] D. Bluvstein et al., *A quantum processor based on coherent transport of entangled atom arrays*, Nature **604** (2022) 451.

[30] V. Lakshminarayanana and A. Fleck, *Zernike polynomials: a guide*,
Journal of Modern Optics **58** (2011) 545.

Acknowledgements

I would like to thank everyone inside and outside the group who helped with this thesis! I would like to especially thank Nina and Lukas, for all the things you have taught me, for your help finding problems in optical setups and Python code, and for proofreading this thesis and improving it with your suggestions; Simon, for your amazing company in the lab; Sebastian, for making it possible for me to write this Bachelor thesis in the group, and for giving a lot of attention to the SLM project; Prof. Meschede for being second corrector and for the optics lecture; Tangi for showing me your setup of an SLM, and your suggestions when I had problems with mine; Richard for pointing me to the theses about SLMs from the Meschede group; Thilina for showing how to set up the microscope; Hannes for suggesting this cool topic; the entire group for always being approachable and helpful, and for the nice lunches, breaks, barbecues, and Friday physics; and my friends and family for your interest in the topic of this thesis, and all your support!